Marine and Petroleum Geology 134 (2021) 105345

Contents lists available at ScienceDirect

Marine and Petroleum Geology

journal homepage: www.elsevier.com/locate/marpetgeo

Mineralogy, microfabric and pore evolution in late-middle Ordovician mudstone of the Utica/Point Pleasant sub-basin of Ohio, West Virginia, and Pennsylvania

Julia M. Sheets [a,*], Susan A. Welch [a], Tingting Liu [a], Edwin R. Buchwalter [a,1], Alexander M. Swift [a], Steve Chipera [b], Lawrence M. Anovitz [c], David R. Cole [a]

[a] School of Earth Sciences, The Ohio State University, Columbus, OH, USA
[b] Chesapeake Energy, Oklahoma City, OK, USA
[c] Chemical Sciences Division, MS 6110, Oak Ridge National Laboratory, Oak Ridge, TN, 37830, USA

ARTICLE INFO

Keywords:
Utica Shale
Point Pleasant Formation
Mineralogy
Microfabric
Porosity
Accessible surface area
Diagenesis
Hydraulic fracturing target

ABSTRACT

The Utica/Point Pleasant Formations comprise a major unconventional gas resource in the Appalachian Basin. Core samples from several boreholes in Ohio, West Virginia and Pennsylvania were studied to determine mineralogy, microtexture/microfabric, accessible pore surface area, porosity and pore size distribution as a function of maturity in the Utica/Point Pleasant sub-basin. This effort compares shallower, generally more phyllosilicate-rich Utica intervals with deeper, more carbonate-rich Point Pleasant intervals, the latter representative of horizons currently targeted for gas recovery. The Point Pleasant Formation contains mostly calcite (in the form of fossil tests, grains, and cements), distributed within alternating carbonate- and phyllosilicate-rich matrix laminae, as well as coarse-grained fossil-rich laminae. In both Utica and Point Pleasant core samples, the greatest mercury-accessible connected porosity measurements are associated with the highest maturity samples, an observation that is particularly pronounced for the Point Pleasant. More detailed vertical sampling and analysis of core from a well in Harrison County, Ohio (a region that has experienced copious shale gas production) shows that surface area, pore volume and pore connectivity increase locally in target horizons identified for gas recovery. Observations suggest that optimal mixtures and arrangements of minerals and organic matter, as well as increasing maturity, contribute to forming this productive carbonate-rich unconventional resource. In particular, early diagenetic calcite and quartz cement and increasing quantities of silt-sized particles are associated with higher measured connected porosities, while later-stage matrix dolomitization and recrystallization of fossil laminae tend to occlude the pore network.

1. Introduction

The impact of organic-rich mudrocks on the American and global energy landscapes cannot be overstated. The application of horizontal drilling and hydraulic fracturing to these formations has allowed the United States to surpass Russia and Saudi Arabia in oil production, producing just over 13 million barrels of oil per day in March of 2020 (EIA Weekly US Field Production of Crude Oil, accessed January 2021 (https://www.eia.gov/dnav/pet/hist/LeafHandler.ashx?n=PET&s=WCRFPUS2&f=W). While US conventional production has seen declines over the past decade, unconventional US onshore drilling and production accounts for nearly all of the production output since 2008 (Sieminski, 2014).

Despite poor commodity prices that began in 2016, energy and production companies continue to invest in several select basins throughout the United States, with continued activity in the Utica and Marcellus shales (EIA Drilling Productivity Report, November 2020). As of 2019, natural gas has become the fuel of choice for electricity production, accounting for 38.4% of all utility scale electricity produced in the United States, well in excess of coal's 23.4% (EIA Monthly Energy

* Corresponding author.
E-mail addresses: sheets.2@osu.edu (J.M. Sheets), welch.318@osu.edu (S.A. Welch), liu.2189@osu.edu (T. Liu), edwin_buchwalter@swn.com (E.R. Buchwalter), swift.63@osu.edu (A.M. Swift), steve.chipera@gmail.com (S. Chipera), anovitzlm@ornl.gov (L.M. Anovitz), cole.618@osu.edu (D.R. Cole).
[1] Current address: *Southwestern Energy, Houston, TX.*

https://doi.org/10.1016/j.marpetgeo.2021.105345
Received 7 February 2021; Received in revised form 13 September 2021; Accepted 23 September 2021
Available online 29 September 2021

Review, November 2020). In Ohio, shale gas production has increased from 84.3 billion cubic feet of natural gas in 2012 to more than 2.6 trillion cubic feet in 2019. These resources have a material impact on the local economies where they are extracted (EIA Ohio Dry Natural Gas Production, accessed December 2020 (https://www.eia.gov/dnav/ng/hist/na1160_soh_2a.htm). Given the profound resurgence of the American domestic energy industry being tied almost exclusively to these organic-rich mudstones, it is likely that these energy resources will continue to shape the future of American domestic energy supplies. Over the past decade, the increased utilization of natural gas (largely displacing coal) for energy generation has significantly decreased US CO_2 emissions, and natural gas infrastructure is projected to be integrated for renewable biogas generation in the future (Mac Kinnon et al., 2018). However, some model scenarios suggest that, given the relatively low cost of natural gas, its increased use may lead to significantly higher greenhouse gas emissions in future decades (Raimi, 2020).

Of fundamental importance to a holistic understanding of unconventional gas resources are the mudrocks that host them. Colloquially referred to as "gas shales," it is now well known that the mineralogical composition and, more importantly—the fabric—of these Earth materials is complex and variable (Macquaker and Adams, 2003; Lazar et al., 2015; Fairbanks et al., 2016; Peng et al., 2020). However, some key elements of hydraulic fracturing targets are similar. Among these are specific mineral/organic matter (OM) arrangements, and the resulting pore networks that comprise the matrix laminae (Swift et al., 2014; Loucks and Reed, 2014). Even for reservoirs with similar fracture permeability and gas content, however, production may be variable, and this has been attributed to rock fabric and mineralogic heterogeneities (Bustin and Bustin, 2012). Therefore, measurements of pore abundance, morphology and size distribution, as well as mineral and OM associations are needed to advance our understanding of rock response to hydraulic fracturing.

This research tests the hypothesis that the mineralogy and microfabric of carbonate-rich mudrocks exert important controls on their suitability as hydraulic fracturing targets (i.e. porosity, which affects gas storage, and permeability, which affects gas recovery). To this end, core samples across the Appalachian basin that include the Utica and Point Pleasant formations (and also Lexington/Trenton in one borehole) were interrogated at centimeter to nanometer length scales using: 1) light and electron microscopy to determine OM/mineral/pore associations, 2) powder X-ray diffraction to quantify bulk mineralogy, and 3) mercury and gas porosimetry to investigate the nature of pores including connected surface area, pore size, and pore volume. Pore-mineral associations were qualitatively interpreted by considering results from all three approaches. We also explored the geological controls (depositional environment, nature of original OM, diagenesis) on the development of the microfabrics observed in the Utica/Point Pleasant samples, with an emphasis on the Point Pleasant calcisiltite hydraulic fracturing target.

2. Utica/Point Pleasant geologic framework

The general term "Utica Shale" refers to all of the OM-rich mudstones in the intervals above the Lexington/Trenton Formation (Patchen and Carter, 2015). Depending on geographic location, these OM-rich mudstones may include, from lowest to uppermost, the Logana Member of the Lexington/Trenton Formation, the Point Pleasant Formation, and the Utica Formation. The Trenton in northwestern Ohio "grades upward and laterally" into the Point Pleasant and these formations are considered to be stratigraphically equivalent in this region (Wickstrom et al., 1992). The Utica/Point Pleasant sub-basin transitions from interbedded limestones and carbonate-rich argillaceous mudstones (deposited in the Point Pleasant Formation) to argillaceous mudstones in the overlying Utica Formation. The transition between the Point Pleasant and the overlying Utica Formation is gradational, and the latter thickens to the east in the Appalachian Basin (Wickstrom et al., 1992, 2012; Patchen and Carter, 2015). While the Utica and Point Pleasant formations are locally correlative, large-scale variations in thickness, porosity, and electronic log responses have been observed and noted in seismic and electronic log data regionally (Patchen et al., 2006; Wickstrom et al., 2012; Bloxson, 2017).

The Utica and Point Pleasant formations were deposited in shallow seas during the Katian stage of the Upper Ordovician period, 453–445 million years ago, at which time the sub-basin was located at about 20° south latitude on the Laurentian plate (Witzke, 1990; Patchen et al., 2006). The sub-basin was flanked by carbonate platforms and carbonate ramp environments to the northwest (Trenton/Black River) and south (Lexington), and the Taconic foreland basin to the east (Patchen et al., 2006). This is consistent with petrographic analysis, which suggests that the sub-basin was adjacent to sources of carbonate debris and high organic productivity (Bloxson, 2017). Fig. 1 shows a map of the sub-basin and adjacent paleogeographic regions during the late middle Ordovician.

The Lexington and Trenton carbonate platforms resulted from the development of a distal bulge brought on by the closing of the Iapetus Ocean during the Taconic Orogeny, with a series of island arcs and mountains emerging to the east of the sub-basin (Faill, 1997; Ettensohn, 2008). The distal bulge allowed for the creation of a vast shallow sea with several dominant carbonate ramps and shelves (Faill, 1997). As shown in Fig. 1, the Lexington platform was the major carbonate production region that developed in modern day Kentucky and West Virginia, while the Trenton/Black River carbonate platform formed in the shallow waters over what is now northwest Ohio and New York (Patchen et al., 2006; Wickstrom et al., 2012). Between these carbonate platforms, the Utica/Point Pleasant sub-basin accommodated the deposition of interlayered carbonate (some clastic) and siliciclastic sediments. Later, the subsiding Taconic foreland basin drowned the carbonate platforms (Patchen et al., 2006).

The Sebree Trough was a narrow area of relatively deeper water between the carbonate platforms that provided a channel to the Iapetus Ocean at the continental margin to the south (Kolata et al., 2001). This channel might have allowed cool, phosphate-rich subpolar water to flow into the Utica/Point Pleasant Sub-Basin. Abundant graptolites and trilobites indicate deposition in deeper water than that along the platform

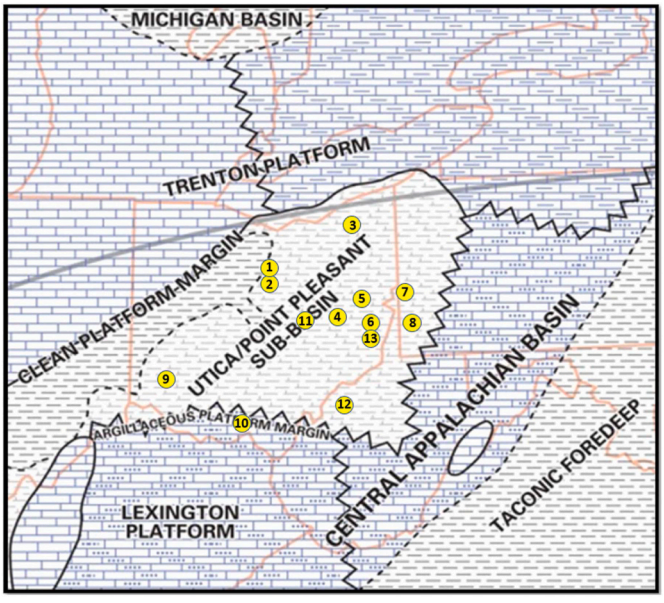

Fig. 1. Utica/Point Pleasant sub-basin during the late middle Ordovician, showing the predominant rock facies across the region. Approximate well locations for core samples studied are shown with yellow circles (base map from Patchen et al., 2006). Numbers correspond to the well numbers given in Tables 1 and 2, below. (For interpretation of the references to colour in this figure legend, the reader is referred to the Web version of this article.)

margins, where brachiopod, bryzoan, and echinoderm fossils are found (Kolata et al., 2001).

3. Materials and methods

3.1. Samples

A suite of core samples and analyses of the Utica/Point Pleasant Fm. from several vertical wells across Ohio and western Pennsylvania were donated by Chesapeake Energy for this project. Two 4-inch diameter cores separated in depth by approximately 100–150 ft (30–50 m) were provided from each well (Table 1). Each pair of cores generally included a phyllosilicate-rich upper sample and a carbonate-rich lower sample. In addition, three samples were obtained from a northern Ohio well (see Table 1, Geauga County). Based on depth and mineralogical composition, the clay mineral-rich upper samples are designated as belonging to the Utica (Ut) Formation, and the carbonate-rich lower samples to the Point Pleasant (PtP) Formation. A second sample suite was provided by Gulfport Energy from a borehole in Harrison County, Ohio near the Belmont/Harrison County line. This allowed more detailed sampling of several depths of the Point Pleasant as well as the underlying Lexington/Trenton Formation (Table 2, Well #13). For this borehole, we are informed by industry about the target depth horizon for condensates and gas, which is the lower horizon of the Point Pleasant formation, depth range ~8490–8550 ft (2588–2606 m).

Several Utica/Point Pleasant core samples also were obtained from the H.R. Collins Lab and Core Repository: Ohio Geological Survey (Table 1). As noted by Witt (1993), Patchen et al. (2006), Ettensohn (2010), and Patchen and Carter (2015), the contact between the Point Pleasant and Utica Formations is gradational across the basin, and both contain interbedded limestones and shales (Potter, 2007). Nonetheless, we attempted to integrate geophysical log measurements with core depths to identify these samples as Utica or Point Pleasant. In particular, interactive well log data that include depths to formation tops provided in the Utica Playbook (Hickman et al., 2015) were used for formation identification.

3.2. Analytical methods

For bulk mineralogy measurements with X-ray diffraction (XRD), two sets of analyses of the Chesapeake samples were acquired from two laboratories. Subsamples of each core were extracted independently at each laboratory so that a different powder sample was measured in each lab. The first set was conducted at Chesapeake Energy. To each powdered rock sample, 1.0-μm corundum (Al_2O_3) internal standard was added in the ratio 80% sample to 20% corundum by weight, and subsequently ground under acetone in a McCrone Micronizing mill (fitted with an agate grinding set) for 10 min. All diffraction patterns were collected on a Bruker D4 X-ray powder diffractometer using CuKα radiation and a Bruker VANTEC position sensitive detector, from 2 to 70°2θ, using ~0.04° steps, and counting for at least 1s/step.

The second set was measured at The Ohio State University (OSU). Powdered samples were prepared by hand grinding in a corundum mortar and pestle. Some were subsequently further ground under isopropyl alcohol for ~5 min in a McCrone Micronizing mill using zirconium oxide grinding media. OSU samples were analyzed with CuKα radiation (45 kV and 40 mA) using a Malvern-PANalytical X'Pert Pro X-ray diffractometer, scanned from 5 to 70°2θ, with 0.02°2θ step size, 2 s per step using either a scintillation detector or a high speed X'celerator detector. The Harrison County Well #13 samples were only analyzed at OSU.

Rock fabric and mineralogy were analyzed at OSU from polished thick sections (~150 μm) of core cut parallel and perpendicular to bedding. A Quanta 250 field emission scanning electron microscope (FE-SEM) was used, equipped with a Bruker energy dispersive X-ray (EDX) spectrometer and Quantax software, and the FEI-ThermoFisher **Q**uantitative **E**valuation of **M**ineralogy with **SCAN**ning electron microscopy (QEMSCAN) analytical platform.

A Zeiss Crossbeam 1540 dual beam (electron and Ga-ion) focused ion beam/scanning electron microscope (FIB/SEM) at the Center for Nanofabrication, Molecular Foundry, Lawrence Berkeley National Laboratory (LBNL) was used to acquire secondary electron (SE) images of FIB slices of selected samples. The Gemini Column of the Crossbeam is equipped with both a standard Everhart Thornley (ET) detector and an Inlens SE detector for high resolution image acquisition (image area approximately 10 × 10 μm^2) per FIB slice. Helium-Ion microscopy of selected samples was conducted using a Zeiss Orion NanoFab at the Center for Nanophase Materials Sciences at Oak Ridge National Laboratory (ORNL-CNMS).

Connected porosity measurements were made at OSU using mercury intrusion capillary pressure (MICP) and N_2 gas sorption analysis. For MICP, samples were cut to produce intact parallelepipeds of similar size and weight (~3–5 g) and interrogated with a Micromeritics AutoPore IV 9500 (software version 1.09) mercury porosimeter. A Micromeritics ASAP 2020 using nitrogen as the sorbate gas was used to obtain gas sorption isotherms. Analyses were initially conducted on intact core chips, but due to the long equilibration times, samples were subsequently gently disaggregated and crushed with a corundum mortar and pestle and sieved to 60 mesh (<250 μm in length scale) before analysis. The goal was to preserve grain sizes amenable to interrogating pore

Table 1
List of Utica and Point Pleasant samples from OH, PA, and WV.

Well #	Formation	Depth (ft)	Location (County; State)	Maturity (Ave. Ro)[b]	TOC (wt. %)
1	Ut	2959	Richland; OH	0.59	4.5
1	PtP	3055	Richland; OH	0.59	3.2
2	Ut	4471	Richland; OH	0.78	2.4
2	PtP	4631	Richland; OH	0.78	4.1
3	Ut	5778	Geauga; OH	1.2	3.2
3	PtP	5878	Geauga; OH	1.2	1.6
3	PtP	5912	Geauga; OH	1.2	3.3
4	Ut	6528	Tuscarawas; OH	1.06	1.9
4	PtP	6644	Tuscarawas; OH	1.06	3.5
5	Ut	6840	Carroll; OH	1.14	1.9
5	PtP	6964	Carroll; OH	1.14	2.6
6	Ut	8334	Harrison; OH	1.62	1.9
6	PtP	8440	Harrison; OH	1.62	3.6
7	Ut	8835	Beaver; PA	2.02	2.2
7	PtP	8985	Beaver; PA	2.02	3.1
8	Ut	10,855	Washington; PA	2.49	1.4
8	PtP	10,930	Washington; PA	2.49	4.1
9	PtP	859[a]	Warren; OH	nd	nd
10	Lex	3240[a]	Scioto; OH	nd	nd
11	PtP	5681[a]	Coshocton; OH	nd	nd
12	PtP	9503[a]	Wood; WV	nd	nd

Calc. %Ro from T_{max} = Calc. %VRo = 0.0180 × T_{max} - 7.16 (Jarvie et al., 2001).
[a] Ohio Geological Survey samples.
[b] At lower maturities, T_{max} was used.

Table 2
List of Point Pleasant, Lexington, and Trenton-Black River samples from a second Harrison County, OH well.

Well #	Formation	Depth (ft)	Location (County; State)	Maturity (Ave. Ro)[a]	TOC (wt. %)
13	PtP	8479	Harrison; OH	~1.6	nd
13	PtP	8482	Harrison; OH	~1.6	nd
13	PtP	8492	Harrison; OH	~1.6	nd
13	PtP	8529	Harrison; OH	~1.6	nd
13	PtP	8549	Harrison; OH	~1.6	nd
13	Lex	8556	Harrison; OH	~1.6	nd
13	Lex	8586	Harrison; OH	~1.6	nd
13	Trn	8605	Harrison; OH	~1.6	nd

[a] Maturity value is assumed to approximate that determined for the Chesapeake Energy Harrison County borehole samples (Table 1, Well #6).

volume and surface area that could be attributed to pores within grains, rather than analysis of external grain surfaces.

Not all measurements were conducted on all core samples; rather, examples were selected that represent a range of maturities. Details of the analytical methods and data reduction used for powder XRD, SEM, QEMSCAN, MICP and N_2 gas sorption are provided in the Supplementary Information (SI): Analytical Methods.

4. Results

4.1. Bulk mineralogy

Powder XRD analysis of the Utica/Point Pleasant core samples from Chesapeake Energy shows they primarily contain calcite, quartz, Fe–Mg illitic clay, muscovite, Fe-rich chlorite (chamosite), dolomite, alkali feldspar (K-feldspar and Na-rich plagioclase), and pyrite. As discussed above, most of the Chesapeake core sample pairs (Table 1) include a shallower Utica that is richer in silicates (mainly phyllosilicates), and a deeper Point Pleasant that is richer in carbonates. A detailed comparison of XRD scans acquired at OSU from these two layers is given in Fig. S1. This higher carbonate content (mainly calcite) for the deeper sample only holds, however, for moderate to high maturity sample pairs (approximate depth range 4470–10930 ft (1362–3331 m); Ro range ~0.78–2.49). It was not observed in the second set of analyses for the lowest maturity pair (Ut 2959; PtP 3055), which shows elevated calcite for the shallow sample and little difference in phyllosilicate content between the two. Table 3 summarizes the results of these measurements quantified using Rietveld analysis with the Malvern-PANalytical HighScore Plus analytical platform (OSU, gray shaded samples), and FULLPAT, a quantitative X-ray powder diffraction (QXRD) program and method (Chesapeake). In most cases for OSU analyses, several Rietveld models were run, and the result that showed the best agreement between the observed and calculated XRD scan (through evaluating the difference plot and agreement indices) was selected. The "f" and "m" labels on core depths from the second Harrison County well in Table 3 refer to fossil-dominated and matrix-dominated subsamples of core, as determined by the unaided eye (see section 4.2. below).

Table 3
Quantitative Mineralogy. Qtz = quartz, Ksp = ordered K-feldspar, Plag = ordered albite, Ap = apatite, Py = pyrite, Mar = marcasite, Cal = calcite, Dol = Ferroan dolomite, I/S = mixed-layer illite/smectite, Chlor = chamositic chlorite or Fe-clinochlore. Carb (carbonates), Q + F (quartz + feldspar), and Phy (phyllosilicates) are renormalized values for ternary diagrams.

Well #	County	Sample	Qtz	Ksp	Plag	Ap	Py	Mar	Cal	Dol	I/S	Ill + Mu	Chlor	Carb	Q + F	Phy
9	Warren	PtP 859	24.2	2.6	4.1	0.0	1.5		20.8	2.9		29.1	14.9	24	31	45
1	Richland	Ut 2959	21.2	1.1	4.7	1.5	1.3		17.4	3.2	4.9	38.2	1.9	22	29	48
1		Ut 2959	19.5	3.6	1.9	0.0	1.1		53.9	5.4		14.1	0.5	60	25	15
1		PtP 3055	17.0	1.3	2.2	1.9	0.9		43.0	5.8	6.2	18.5	0.1	52	22	26
1		PtP 3055	19.5	0.0	0.0	0.0	0.5		55.5	8.8		14.1	0.0	66	20	14
10	Scioto	Lex 3240	18.6	3.8	0.0	0.0	2.6		23.0	2.8		40.5	7.2	27	23	50
2	Richland	Ut 4471	23.6	1.1	3.7	0.6	2.6		18.9	3.4	2.9	37.9	2.9	24	30	46
2		Ut 4471	16.4	0.0	0.0	0.0	1.0		56.2	9.6		16.2	0.7	66	17	17
2		PtP 4631	11.2	1.4	2.0	1.8	0.9		54.7	2.8	6.3	14.7		62	16	22
2		PtP 4631	15.1	1.1	0.8	0.0	0.6		68.3	2.7		11.3	0.0	72	17	11
11	Coshocton	PtP 5681	20.0	0.0	2.4	0.0	0.7		61.3	5.5		10.1	0.0	67	23	10
3	Geauga	Ut 5778	19.0	0.4	3.4	0.8	1.1	0.4	23.3	7.8	4.5	33.5	2.6	33	24	43
3		Ut 5778	23.1	0.0	1.4	0.0	0.7	0.0	36.3	14.3		20.5	3.7	51	25	24
3		PtP 5878	10.9		0.8	0.5	0.4		75.6	3.7		6.4		81	12	7
3		PtP 5878	11.5		0.0	0.0	0.0		83.7	4.8		0.0	0.0	89	12	0
3		PtP 5912	7.7		1.3	0.8	0.9		61.2	5.5		19.2		70	10	20
3		PtP 5912	8.0		0.0	0.0	0.0		79.6	5.6		6.7	0.0	85	8	7
4	Tuscarawas	Ut 6528	19.9	0.8	4.3	0.8	1.7	0.4	12.6	3.7	4.4	44.7	4.8	17	26	57
4		Ut 6528	7.5	0.0	3.4	0.0	1.9	0.0	21.7	3.1		52.5	10.0	25	11	64
4		PtP 6644	14.2	0.8	1.5	1.3	0.9	0.4	53.5	3.7	5.0	15.1	0.1	61	18	22
4		PtP 6644	16.4	0.0	3.0	0.0	1.2	0.0	64.2	3.6		0.0	11.4	69	20	12
5	Carroll	Ut 6840	21.9		5.3	1.0	1.7		13.7	2.2	5.8	42.2	4.1	17	29	55
5		Ut 6840	24.1		3.9	0.0	2.0		17.4	1.8		45.3	5.5	20	29	52
5		PtP 6964	7.5		1.2	1.4	0.7		66.6	3.0	5.9	11.1		73	9	18
5		PtP 6964	11.5		2.0	0.0	1.0		66.8	3.1		15.6	0.0	71	14	16
6	Harrison	Ut 8334	20.4	0.7	5.5	0.9	1.7		11.1	3.2	5.1	41.8	7.7	15	28	57
6		Ut 8334	23.0	0.0	1.7	1.0	0.0		8.9	4.1		52.8	8.5	13	25	62
6		PtP 8440	17.9	1.3	3.9	1.3	1.3		45.3	4.0	4.5	16.6	0.5	53	25	23
6		PtP 8440	23.0	0.0	2.5	0.0	1.1		55.3	3.4		14.8	0.0	59	26	15
7	Beaver	Ut 8835	20.6	0.7	4.8	1.5	2.6		17.2	3.9	5.5	37.6	3.6	22	28	50
7		Ut 8835	25.8	0.0	1.9	0.0	1.1		10.7	1.6		46.6	12.3	12	28	60
7		PtP 8985	10.4	0.8	2.1	0.5	1.3		58.9	3.8	4.2	14.8		66	14	20
7		PtP 8985	8.6	0.0	2.5	0.0	0.6		80.7	2.2		5.4	0.0	83	11	5
12	Wood	PtP 9503	25.4	0.0	10.4	0.0	3.3		14.9	2.0		32.1	10.2	18	38	45
8	Washington	Ut 10,854	21.3	0.9	4.4	0.4	1.9		13.2	2.1	5.4	41.2	7.7	16	28	56
8		Ut 10,854	21.5	0.0	2.5	0.0	1.6		11.3	1.0		54.2	8.4	12	24	63
8		PtP 10,930	14.8	1.0	3.9	0.9	1.2		49.5	2.8	4.3	17.1	0.3	56	21	23
8		PtP 10,930	16.6	0.0	5.0	0.0	1.3		61.9	5.1		10.1	0.0	68	22	10
13	Harrison	PtP 8479 f	8	0	4	0	1		82	3		2		86	12	2
13		PtP 8479 m	15	0	5	0	1		63	6		9	1	70	20	10
13		PtP 8482 f	22	0	4	0	1		54	2		12	5	57	26	17
13		PtP 8482 m	25	0	4	0	2		27	3		34	5	31	30	40
13		PtP 8492	19	0	6	0	2		57	1		10	5	59	26	15
13		PtP 8529	34	0	8	0	3		37	3		8	8	41	43	16
13		PtP 8549	15	0	3	0	2		58	5		17	1	64	18	18
13		Lex 8556	14	0	0	5	3		61	4		7	6	71	15	14
13		Lex 8586	10	0	3	3	1		72	1		7	3	76	14	10
13		Trn 8605	11	0	6	0	2		39	9		25	8	49	17	34

4.1.1. Utica

A comparison of all the phyllosilicate-rich (Utica) samples shows notable differences in mineralogy. For example, in the low-maturity core from Richland County (Ut 2959′), the weight percent of albite is less than that in the higher maturity samples, and most of the alkali feldspar is K-feldspar. Overall carbonate content (calcite + dolomite) generally decreases with depth/maturity, while silicate content (chlorite (chamosite) + illitic clay + quartz + albite) increases (Fig. S2). A mid-maturity sample from Geauga County, which may have been geothermally altered (Ut 5778, Ro = 1.2) also has a relatively high dolomite content. In addition, Utica samples measured without a graphite monochromator all show a higher Fe fluorescence generated by Bremsstrahlung radiation than their co-located, underlying Point Pleasant samples measured similarly. This is due to a higher Fe concentration in the Utica Formation, generally in pyrite, chlorite, and illitic clay, which produces more Fe fluorescence in the CuKα X-ray measurements. The only exception to this trend is the lowest maturity pair (Ut 2959 and 3055) which show the same low iron fluorescence.

4.1.2. Point Pleasant

Among the carbonate-rich (Point Pleasant) samples, differences in mineralogy as a function of depth are more subtle. Fe-rich chlorite (chamosite or Fe-clinochlore) was not detected by XRD, indicating its absence or low abundance (~1 wt %). However, a 10-Å phyllosilicate (e.g. illitic clay or muscovite) was observed in all Point Pleasant XRD scans. The weight percent dolomite was highest in the shallowest Richland County Point Pleasant (PtP 3055), the OGS Coshocton County well (PtP 5681), and Geauga County (PtP 5912). A qualitative comparison of Point Pleasant XRD scans for low, moderate and high maturity core samples is shown in Fig. S3.

4.1.3. Vertical sampling well

In the Harrison County, OH well with more detailed sampling of the Point Pleasant (Table 2) the weight percent of silicates (mainly illitic clay and quartz) increased toward the base of the formation and near the hydraulic fracturing target (Fig. 2). In addition, well cuttings showed an abrupt mineralogical transition between the Utica and Point Pleasant, much like results from the Chesapeake Energy wells. Apatite was also detected in XRD scans of the underlying Lexington/Trenton Formation.

Fig. 2 summarizes the major mineralogical trends observed in the first set of XRD measurements of co-located Utica and Point Pleasant samples from Chesapeake (Table 3) and the vertical sampling well in Harrison County, Ohio. As expected, Utica Formation samples trend toward the phyllosilicate apex of the ternary, while Point Pleasant Formation samples trend toward the carbonate apex. The Harrison County Well #13 samples also plot in a generally carbonate-rich field, although the variability in silicate content extends the datafield for this well.

A ternary plot of the mineralogy of the second set of analyses of Chesapeake cores, along with those from the four Ohio Geological Survey samples (see Table 1) are shown in Figs. S4, S5. These show more mineralogical variability, with some Point Pleasant samples plotting in a region generally expected for the phyllosilicate-rich Utica, and vice versa. Better agreement for the two labs was obtained for the higher maturity Chesapeake samples (Table 3).

4.2. Composition of the microfabric

SEM analysis of polished sections shows that the Utica and Point Pleasant samples are argillaceous sparse biomicrites (Folk, 1959, 1962; Flügel, 2010) or, following the Milliken (2014) classification, calcareous argillaceous mudrocks (CARL). Except for the lowest maturity samples, they are all strongly laminated and contain largely intact fossils (mostly silt-to sand-sized). Some fossils form narrow laminar beds, while others occur as individual, widely dispersed shells floating (Flügel, 2010) in the rock matrix.

Parts of core that are laminar and fine-grained are referred to as *matrix dominant.* These can be further separated into carbonate-rich and silicate-rich laminae (the latter mostly phyllosilicates and quartz). Fig. 3 shows images of this mineralogical variation in the highest maturity Point Pleasant sample from western Pennsylvania (PtP 10,930). The smallest clay-sized matrix grains are best distinguished by SEM BSE imagery and EDX spot analyses, while grains larger than 1 μm are

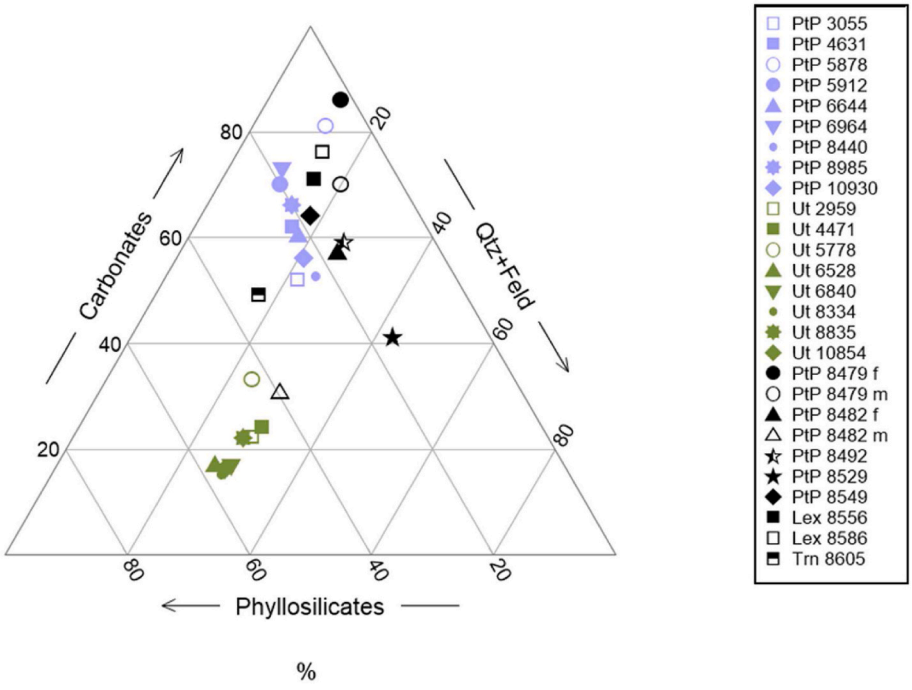

Fig. 2. Rietveld mineralogy in weight percent, renormalized and plotted with apices: carbonates, phyllosilicates, quartz + feldspar. Green symbols - Utica; purple symbols - Point Pleasant. Black symbols are from the Harrison County Well #13 with more detailed vertical sampling. (For interpretation of the references to colour in this figure legend, the reader is referred to the Web version of this article.)

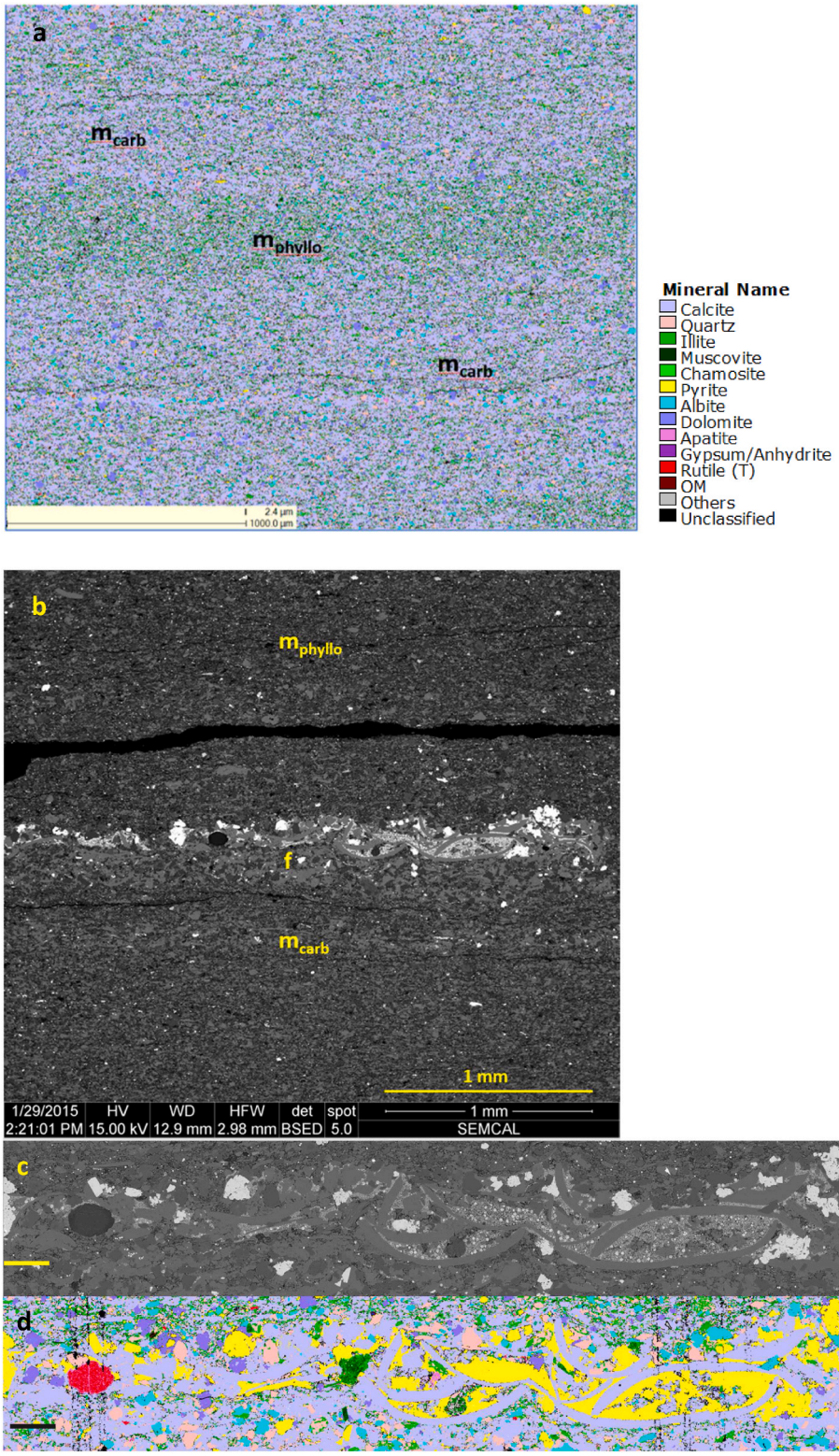

Fig. 3. a) Large (3 × 3 mm) QEMSCAN matrix field showing alternating carbonate- and phyllosilicate-rich matrix domain mineralogy among silt- and clay-sized matrix layers. Coarser layers (lavender) contain fewer phyllosilicates. b) Low magnification, contrast enhanced SEM BSE image, close to the same scale as field a), showing major microfabric components of the Utica/Point Pleasant core samples studied, section cut approximately perpendicular to bedding: "m_{phyllo}" and "m_{carb}" are matrix-dominated (silt and clay sized) laminae, "f" is mostly sand-sized fossil skeletal lamina. c) BSE and d) QEMSCAN showing detail of fossil test structure and mineralogy (scale bar = 100 µm). The large (~100 µm) oval peloidal grain, dark in BSE image c) and fuchsia in QEMSCAN image d), is interpreted as a fecal pellet. Highest maturity polished core section, PtP 10,930, Washington County, PA.

readily visible in QEMSCAN mineral maps (Fig. 3 a, d). Phyllosilicate-rich lamellae are denoted m_{phyllo} (green zones Fig. 3a), and carbonate-dominated laminae are denoted m_{carb} (lavender zones in Fig. 3a). Calcite, present as both fossil skeletal and fine matrix grains, is the major carbonate. Ca-phosphate (fuchsia) is relatively more abundant in m_{carb} zones, while m_{phyllo} zones tend to contain more pyrite (yellow). Grain sizes are typically coarser but variable in the m_{carb} zones (Fig. 3 a, b), and several other fine-grained minerals are dispersed among clay-to fine silt-sized calcite particles (1–10s of µm in length) in the matrix including illitic clay, quartz, albite, dolomite, chlorite, pyrite, and Ca-phosphate.

Other parts of core, referred to as *fossil dominant,* contain coarser-grained bands composed mostly of fossil materials (labeled "f" in Fig. 3 b). These fossil tests are 100s of microns to millimeters in dimension, and often are visible to the unaided eye. Dolomite, pyrite,

quartz, Ca-phosphate, and albite occur within these bands as large grains and crystals (10s–100s of microns in length), some of which have partially replaced the fossil grains (Fig. 3 c, d). Details of the "m" and "f" domains are shown in low magnification SEM BSE and QEMSCAN imagery in Fig. 3 b, c, d.

These major lithological components are recognizable in all samples studied, although with some variation among samples. Fig. S6 shows X-ray computed tomography images of Point Pleasant sample PtP 4631, showing matrix and fossil laminar domains at the core scale (mm to cm length-scale repeats).

4.2.1. Matrix laminae

Both Utica and Point Pleasant core samples show a finely laminated rock matrix fabric that preserves sand, silt, and clay-sized particles, as well as microfossils and large OM structures that are mainly intact, suggesting a relatively quiet water depositional environment. Rock laminae also are mainly intact, even where originally deformed as soft sediment, including the occasional burrow (rare) or fossil test (more common) that locally disrupted the horizontal orientation of matrix grains and cement. An example of differential compaction of a vertically-oriented fossil structure (rigid) and surrounding matrix grains (compacted more) aligned at various angles to bedding is shown in Fig. S7. The resulting variable orientations of grains around the fossil are preserved, suggesting that later compaction did not obliterate major laminar components.

Viewed in thin sections cut approximately *perpendicular* to bedding, m_{carb} domains contain coarser-grained calcite layers separated by thinner illite (and other clay-sized mineral) laminae (Fig. 3 a, above), which stand out in images acquired from unpolished sample surfaces (Fig. S8 a). This suggests that m_{clay} laminae were compacted more severely during burial. In *horizontal* sections (core cut approximately parallel to bedding), coarse-grained calcite, often very porous, is interspersed with fine-grained pockets of illite and other clay-sized minerals. At least to some extent, these "clay pockets" have preserved primary porosity (Fig. S8 c, d). This bedding-parallel fabric has a more isotropic grain arrangement (Fig. S8 b) than the bedding-perpendicular sections. Core samples of low, moderate, and high maturity (Ut 2959, PtP 6644, PtP 8440) all show this same general bedding-parallel texture.

Further, when observed in bedding-parallel sections, the calcite cement is platy to the point that it resembles illitic clay folia (Fig. S8 c). Spot microanalysis shows that much of this carbonate contains minor Mg and Sr, and is electron-beam sensitive, suggesting it may be poorly crystalline. In addition, these sections show variably oriented clay minerals, with some clay folia parallel to bedding surfaces and others tending toward vertical as they wrap around less ductile mineral grains. This is most evident for illitic clay-rich regions that contain holes resulting from sample prep-plucked pyrite crystallites, around which clay folia tend to wrap. Although porosity in the calcite cement is noted in both vertical and horizontal sections, it is more obvious in the latter where intact material spans more surface area subparallel to bedding. Silica is another important cement observed in bedding-parallel sections (Fig. S8 b). It often replaces calcite and, much like the Mg–Sr calcite, it can be electron-beam sensitive if not fully crystalline—i.e., retains amorphous-like properties (cf. Anovitz et al., 2015).

Many carbonate cements, as well as silt- and clay-sized matrix grains, are partly dolomitized. This is best developed in the least mature (Ut 2959 and PtP 3055) and an intermediate-maturity sample pair (Ut 5778 and PtP 5878), both from northern Ohio (Richland and Geauga counties, respectively). Dolomite euhedra are much less sensitive to e-beam damage than the platy calcite cement. This was most obvious in horizontal sections. Zoned dolomite is less abundant in the high-maturity samples. Fig. S8 d shows corners and edges of dolomite euhedrons engulfing matrix grains. Clay-sized phyllosilicates became incorporated as inclusions into the euhedra as they grew, creating inherited pore space within the dolomite. Such pores are, however, likely to be isolated from the connected pore network.

Although minor in abundance, several forms of Ca-phosphate were identified in Utica and Point Pleasant samples: fossil tests intergrown with OM, nano-crystalline peloidal forms also rich in carbon, and OM-free fluorapatite grains. Fig. S8 d shows a skeletal fragment composed of intergrown fluorapatite and pyrite, a common trace phase dispersed in matrix laminae. Rarely, silt-sized rounded calcite grains are rimmed with Ca-phosphate. These are interpreted as replacement coatings on reworked carbonates that may have formed on or near an ancient erosional surface (Fig. S9). Ca-phosphate also occurs as several large-scale forms, including apparently unaltered fossil skeletal material 100s of microns in size. These appear to be more abundant in the shallow (low maturity) Utica and Point Pleasant samples (Fig. S10).

4.2.2. Fossils

In fossil-rich "f" laminae, the skeletal grains are generally coarser (silt-to sand-sized) than those in matrix laminae (clay-to silt-sized), with individual fossils largely intact (Fig. 3 c, d). These thin fossil beds range in thickness from 100s of μm to millimeters, and are composed mainly of brachiopods, echinoderms, trilobites, and ostracods, among others. Fossil grain boundaries adjacent to matrix are commonly coated with framboidal pyrite. Where organisms trapped mud, fluids, and gases inside their shells at or near the sediment-water interface, the rock that eventually formed retains remnants of partially cemented matrix mud, recrystallized calcite, framboidal pyrite, and recrystallized pyrite of cubic and octahedral habit. Large euhedral pyrite crystals (Fig. S11) follow preferred orientations within the calcite. These large crystals partly replaced originally finer-grained carbonate, demonstrating diagenetic recrystallization. Partially engulfed by the leading edges of pyrite euhedrons, some framboidal pyrite crystallites clearly pre-date the pyrite euhedrons that are mostly cubic {100} in habit. In the deepest Point Pleasant sample studied, PtP 10,930, ion mill-induced chiseling, and in some cases nearly perfect beveling, accentuated tight grain boundaries and emphasized the much greater mechanical strength of the fossiliferous material as compared to the carbonate matrix grains and cement. Silt-sized carbonate-apatite peloids (Fig. 3 d, ~100 μm rounded fuchsia grain) also are preserved within these fossil microbeds in close proximity to the fossil tests and are interpreted here as fecal material. They are similar in size, composition and habit to microcrystalline carbonate-phosphate grains (50–300 μm) recovered from phosphate-rich deposits on the western continental shelf of Africa (cf. Baturin, 1981).

4.2.3. Organic matter

Analysis of OM in the Utica and Point Pleasant cores yielded total organic carbon (TOC) values ranging from ~1.6 to 6.2 wt %. TOC neither correlates with depth/maturity nor occurrence within Utica or Point Pleasant intervals. OM is readily observed in SEM images of all samples, and varies in size, mineral association, and morphology.

OM stringers 10s–100s of μm in length are ubiquitous and occur largely parallel to bedding (Fig. 4 a, d, e). The thickness of these large macerals, as viewed in sections cut perpendicular to bedding, is remarkably constant (approximately 10–30 μm). They are observed in the clay- and silt-sized matrix of all Utica and Point Pleasant samples and are large compared to the surrounding matrix minerals. This class of OM is commonly embayed by euhedral calcite and dolomite. The strongest rock fabric association for these larger macerals is with silt-sized matrix minerals, where the OM bends around adjacent, structurally rigid, grains of calcite, dolomite, quartz, and pyrite (Fig. 4 a, e). In the low-maturity Utica sample (SW 2959), this large OM defines rock bedding in polished sections. Otherwise, the isotropic morphologies of silt-sized matrix calcite, quartz, and dolomite tend to obscure bedding laminae. SEM imagery shows that these OM objects are non-porous.

A second type of OM is several micrometers or less in length scale and intimately associated with illitic clay. Compared to the large OM, most of this "matrix supported" OM has SEM-visible pores with diameters of 10s–100s of nm (Fig. 4 b). This small porous OM also is strongly

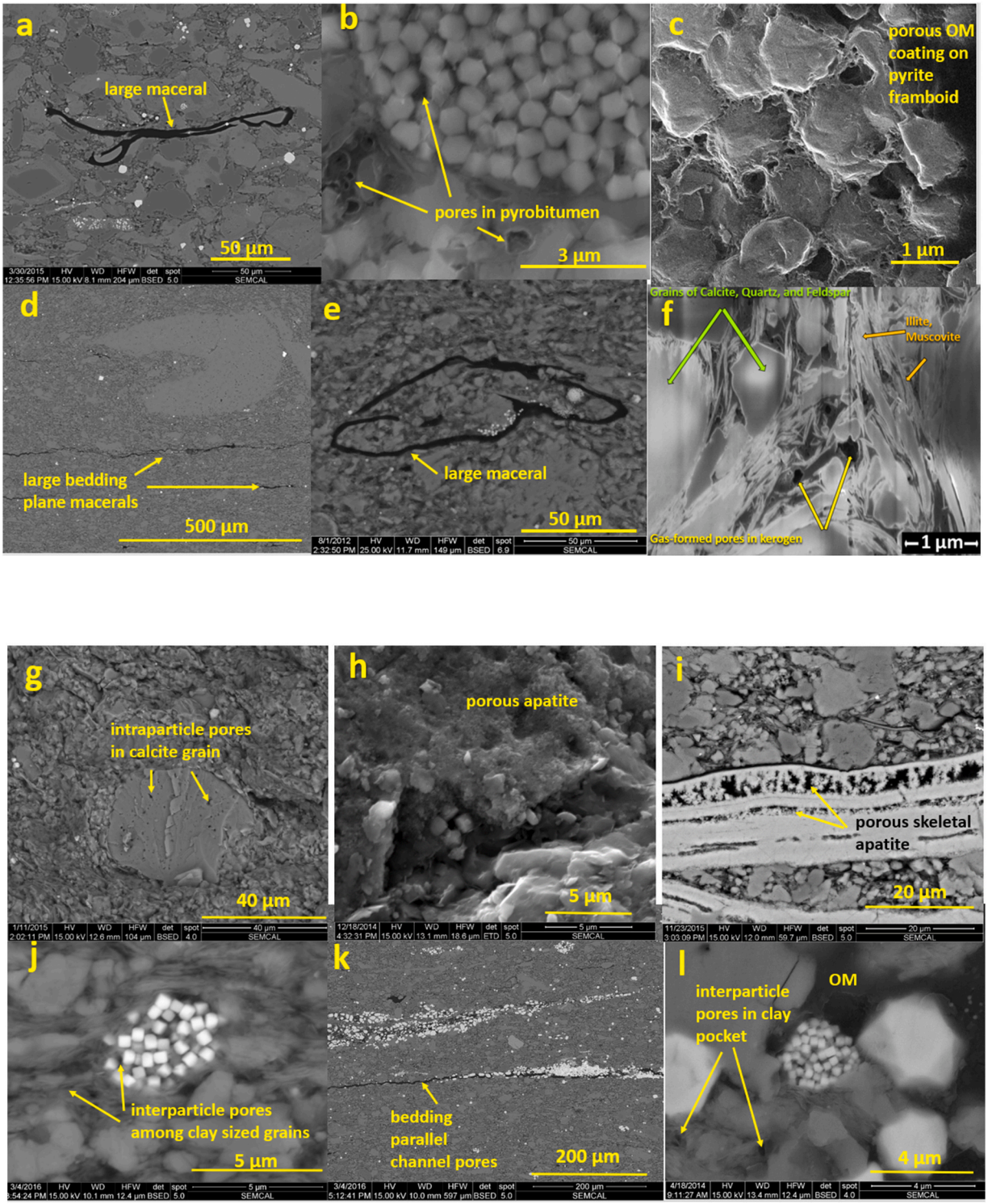

Fig. 4. Representative examples of common microfabric elements in Utica and Point Pleasant core samples, as observed in SEM BSE, HIM, and dual beam FIB/SEM imagery. Images a-f show mineral/organic matter associations. a) Large OM stringer in partially dolomitized matrix (Ut 5778). b) porous matrix-supported OM (interpreted as pyrobitumen based on maturity) (PtP 10,930). c) Pyrite framboid with porous OM coating (PtP 10,930). d) Large bedding-parallel OM stringers in matrix (PtP 8549). e) Large OM surrounding fine silt and clay-sized particles in matrix (PtP 5641). f) Clay pocket with porous matrix-supported OM (PtP 10,930). Images g-l show pore types. g) Intraparticle pores in silt-sized calcite grain (PtP 8550). h) Intraparticle pores in "spongy-textured" apatite (PtP 8492). i) Intraparticle meso-to macropores in skeletal apatite (PtP 8550). j) Interparticle pores between illite and other clay-sized mineral grains (PtP 8529). k) Large cluster of pyrite and celestite crystals and OM occupying bedding-parallel fractures, or "channel pores" (PtP 8529). l) OM (dark), pyrite (euhedral, bright), illite (layered folia, calcite (medium gray) in a clay pocket (horizontal section: Ut 2959).

associated with framboidal pyrite (Fig. 4 c). In fact, pyrite wrapped with illitic clay and coated with OM is a fundamental OM-mineral-pore association in the Utica and Point Pleasant samples. Other clay-sized minerals were observed in contact with this type of OM, but illitic clay interwoven with the organic matter (Fig. 4 f) is the strongest OM-mineral association.

A third type of OM revealed by EDX microanalysis is fine-grained OM intermixed with phosphate and carbonate in the fecal (peloidal) grains described above (Fig. 3 d). Thus, phosphates (CFAs), in addition to clay minerals, are an important mineral group for intimately intermingling with OM. These spheroid-shaped OM particles form topographic lows in polished sections, indicating a susceptibility to mechanical polishing. Other examples of OM associated with phosphate are skeletal phosphate tests containing large pores filled with OM.

4.2.4. Pores

SEM analysis is advantageous, even though limited in terms of the sample volume interrogated, as it provides a means of directly associating pore size and shape with particular minerals or assemblages within the rock fabric. Fig. 4 shows key pore types and their associations in the Utica and Point Pleasant samples. Following the mudrock pore terminology of Loucks et al. (2012), both intra- and inter-particle pores are observed in all core samples. The most obvious *intraparticle* occurrences are meso- and macropores (Sing et al., 1985; Thommes et al., 2015) in matrix-supported OM, silt-sized calcite (both reworked carbonate grains (Fig. 4 g) and cement), silt-sized Ca-phosphate (Fig. 4 h), and sand-sized skeletal grains (large fossil in Fig. 4 d). Intraparticle pores in carbonates and phosphates are easily identified both in small core fragments (Fig. 4 g, h) and polished sections (Fig. 4 d, i). Further, as discussed above, inherited "relict pores" within dolomite cements formed where dolomite euhedrons engulfed clay-sized matrix grains (Fig. S8 d).

Matrix-supported OM pore occurrences are strongly associated with illitic clay and framboidal pyrite, and are located between clay packets or individual pyrite framboid crystallites (Fig. 4 c, f). Samples of widely variable maturity contain OM with pores 10s–100s of nm in diameter (meso-to macropores), although they are most obvious in the highest maturity samples. It is not known whether micropores occur in the small, matrix-supported OM particles, as pores < 5–10 nm are difficult to resolve with SEM. Ion-milled large elongate OM particles are apparently non-porous, at least at the 5–10 nm SEM resolution (Fig. 4 a, e).

Interparticle pores are observed in fine-grained matrices between illitic clay packets, between crystallites comprising pyrite clusters, and at clay- and silt-sized grain boundaries between other phyllosilicates (chlorite, muscovite), carbonate (calcite and dolomite), pyrite, albite, quartz, and Ca-phosphate (Fig. 4 j). Such matrix-domain pores are difficult to characterize without ion-milled surfaces, as grains (particularly pyrite) tend to pluck during mechanical polishing. However, preserved pores are observed in helium ion microscopy (HIM) images (Fig. 4 c) and SEM imagery of ion-polished surfaces (Fig. 4 f).

4.3. Connected porosity measurements

MICP and nitrogen gas sorption analyses interrogate connected pores in a sample. Pore sizes measured range from about 1.7 nm (Sing et al., 1985; Kuila, 2013; Thommes et al., 2015) to 10s of μm, spanning approximately five orders of magnitude in size. MICP measurements for cores from the Utica and Point Pleasant suite (Chesapeake Energy) are shown in Fig. 5. An effort was made to subsample core representative of the overall matrix, rather than that rich in large fossil laminae. This ensured that the material interrogated represents a "bulk matrix" that combines both m_{carb} and m_{phyllo} zones, but intentionally excludes "large fossil" f zones (Fig. 3 c, d). In addition, all MICP samples were cut to parallelepipeds of similar shape and weight to minimize surface roughness or differences in the number of particles comprising the samples, allowing better comparison of results (Buchwalter et al., 2015; Buchwalter, 2016Buchwalter et al., 2015; Buchwalter, 2016). Long equilibration times (1000 s per pressure step) were used to allow intrusion into the pore throats of these low permeability materials.

Fig. 5 a shows MICP pore size distributions determined for Utica cores, and Fig. 5 b shows MICP pore size distributions for Point Pleasant cores. The inset graphs are the corresponding cumulative porosity (ϕ) curves. The cumulative connected porosity plot for PtP 10,930 (high maturity 2.49 Ro) indicates it contains more than five times the connected porosity of PtP 3055 (low maturity 0.59 Ro). Thus, the Hg-accessible connected porosity increases with maturity in both the Utica and the Point Pleasant core samples and is much greater overall in the carbonate-rich Point Pleasant. Moreover, in high-maturity samples, connected porosity is accessed through slightly smaller pore throats in the phyllosilicate-rich Utica core samples (Fig. 5 a). The exception is the lowest maturity depth pair (Ut 2959 and PtP 3055), which show similar MICP results for both Utica and Point Pleasant samples (and similar mineralogy).

N_2 gas sorption measurements, including complete adsorption/desorption isotherms, were acquired for intact rock chips (mm in

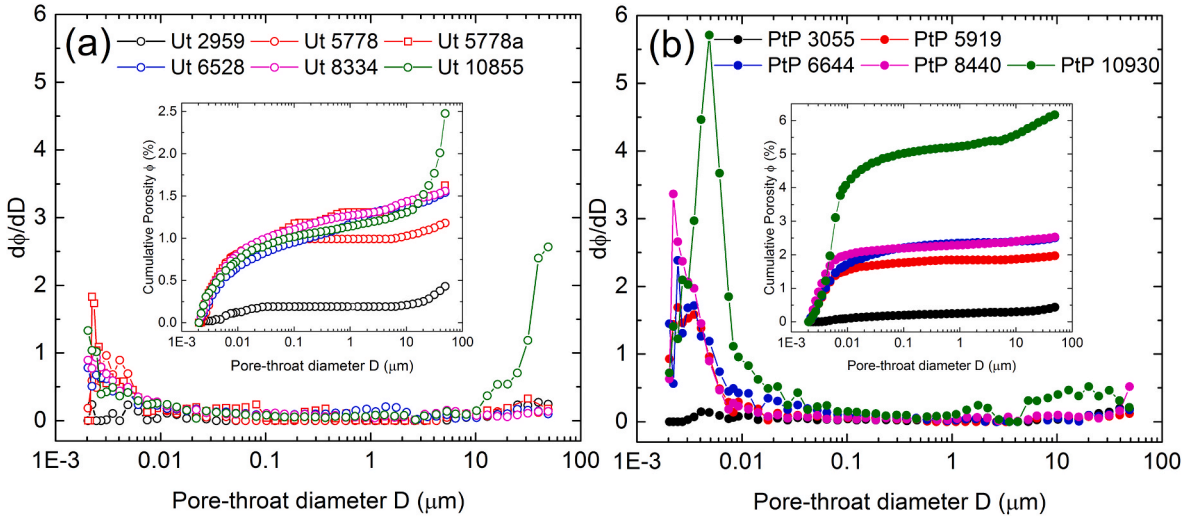

Fig. 5. MICP pore size distributions and cumulative porosity measurements (inset graphs) for Chesapeake Energy depth pairs. a) Utica and b) Point Pleasant represent a range of depths/maturities across the Appalachian basin. Hg-accessibility increases with increasing maturity in both formations, but to a much greater extent for calcite-rich Point Pleasant samples.

dimension) and gently disaggregated powders sieved to <250 μm (60-mesh) for several Utica and Point Pleasant samples (Table 4). However, except for the most mature Point Pleasant sample (Washington County, PA, PtP 10,930) most of the isotherms acquired from rock chips yielded poor results. This observation is in agreement with Mastalerz et al. (2017) who show that rock chunk shale samples from the Illinois Basin greater than ~5 mm (4-mesh) are not suitable for low pressure gas sorption analysis. Although these authors suggest that grain sizes <70 μm (200-mesh) are optimal for shale (Mastalerz et al., 2017), the <250 μm size fraction was used in this study to avoid disaggregating the pore structure, especially because silt sized grains 10s of μm and sand-sized grains 100s of μm are known to exist in the samples (see Section 4.2, above).

Samples designated −02 and −03 (Table 4) were disaggregated powders of intentionally large mass (~5 g) analyzed in order to improve results for low surface area materials. These were gently degassed over long periods to ensure complete sample degassing (Kuila, 2013; Kuila and Prasad, 2013). Low and moderate maturity samples (Ro ~ 0.59–1.06) were degassed at 50 °C for up to 72 h to prevent changes to the OM with heating. Higher maturity samples (Ro ~ 1.62–2.49) were degassed at 100 °C for 12 h.

Plots of surface area, pore volume, and maturity with depth, as well as representative N_2 gas isotherms resulting from the 60-mesh powder samples of Point Pleasant core are shown in Fig. 6 a, b, c, and d, respectively. Fig. 6 d shows that, with increasing maturity, Point Pleasant isotherms have increasingly steep slopes at low relative pressures, suggesting the development of more abundant connected microporosity at higher maturities. In addition, the development of hysteresis loops, most clearly in samples PtP 8440 and PtP 10,930, indicates the presence of mesopores (cf. Type IV isotherms, Thommes et al., 2015). Further, the large increase in gas adsorption at the high P/P_0 range (Type II isotherms) is characteristic of the presence of macropores. As pointed out by Kuila (2013), type IIB isotherms described by Rouquerol et al. (1998) are characteristic of mudrocks. Such isotherms are characterized by hysteresis loops that do not plateau in the high P/P_0 pressure range, and they typically result from adsorbates composed of platy particles or slit shaped pores (Rouquerol et al., 1998).

Interestingly, the most mature Point Pleasant sample from Washington County, PA (PtP 10,930) did yield good gas sorption data from a chip because of a better developed interconnected pore network. Generally, surface area and total pore volume increased with increasing thermal maturity (Fig. 6 a, b, c). One notable exception to this trend was PtP 859 from Warren County Ohio, a low maturity Point Pleasant sample with a surface area and pore volume similar to high maturity Point Pleasant samples (Table 4). Other exceptions are the moderate maturity Ut 5778 and PtP 5878 samples, which show relatively low surface areas and pore volumes, comparable to those of PtP 3055. These samples also show strong dolomitization in quantitative XRD and SEM BSE imagery. For clarity, only the 60-mesh Point Pleasant sample results are plotted in Fig. 6.

Table 4
N_2 gas sorption measurements of select Chesapeake and OGS samples.

Location (county, state)	Sample	Depth (feet)	BET SA (m^2/g)	Maturity (% Ro)	Pore Volume (cm^3/g)
Warren, OH	PtP 859[a]	859	7.6	nd	0.017
Richland, OH	PtP 3055-02	3055	1.7	0.59	0.010
Richland, OH (2)	PtP 4632-02	4632	1.9	0.78	0.008
Geauga, OH	Ut 5778[a]	5778	0.9	1.20	0.003
Geauga, OH	PtP 5878[a]	5878	0.5	1.20	0.002
Coshocton, OH	PtP 5681[a]	5681	5.3	nd	0.002
Tuscarawas, OH	PtP 6644-02	6644	3.6	1.06	0.016
Harrison, OH	PtP 8440	8440	4.7	1.62	0.018
Harrison, OH	PtP 8440-03	8440	5.6	1.62	0.018
Beaver, PA	PtP 8985	8985	4.6	2.02	0.017
Beaver, PA	PtP 8985-02	8985	6.3	2.02	0.017
Wood, WV	PtP 9502[a]	9502	9.4	nd	0.008
Washington, PA	PtP 10,930[a]	10,930	9.5	2.49	0.015
Washington, PA	PtP 10,930	10,930	11.7	2.49	0.025
Washington, PA	PtP 10,930-03	10,930	13.7	2.49	0.024

[a] Denotes rock chip sample.

To obtain a better understanding of vertical relationships, the entire suite of core samples from a single vertical bore hole in Harrison County, OH near the Belmont County line (Table 2, well #13) was assessed by both MICP and N_2 gas sorption. Following Furmann et al. (2016), who conducted a study of OM-rich mudrocks from Alberta, Canada, the following models were used for N_2 gas sorption data reduction: (1) N_2 pore volume is that measurable using the Barret-Joyner-Halenda (BJH) model with the Harkins-Jura (HJ) model of surface thickness, and is taken to include pore sizes from 1.7 to 300 nm. (2) Micropore volume was determined with the Dubinin–Astakhov (DA) model, with an optimized exponent, using relative pressures from 1×10^{-4} to 1×10^{-2} P/P_0. (3) Mesopore volume was determined using the BJH model/HJ model. (4) Macropore volume is the total N_2 adsorption volume minus the micropore and mesopore fractions. (5) Surface area was determined with Brunauer-Emmett-Teller (BET) analysis using the Harkins-Jura model. (6) Micropore surface area is determined with the DA model (Kuila, 2013; Furmann et al., 2016).

Fig. 7a shows that porosity increases systematically with increasing depth in the Point Pleasant, and then drops off by about one-third in the Lexington/Trenton Formation. Within the Point Pleasant, nitrogen-accessible porosity increases from an estimated average of ~4% in sample PtP 8479 to ~7.9% in PtP 8549 at the base of this stratigraphic unit. Mercury-accessible porosity shows the same general trend, increasing from an average of 2.2% in sample PtP 8479, to 5.9% in PtP 8529 but then decreasing slightly to 4.7% in PtP 8549. As shown in Fig. 7 b, mesopores and macropores dominate the connected porosity.

According to lithologic logs, the depths for these Harrison County, Ohio core samples fall within the Point Pleasant Formation and the Lexington/Trenton/Black River limestones. Based on available well log data, samples PtP 8492 and PtP 8529 straddle the target hydraulic fracturing intervals within the Point Pleasant. The silicate content of the samples varies, with depths 8482′matrix, 8492′, and 8529′ having more quartz, phyllosilicates (illitic clay/muscovite and chlorite) and albite (Fig. 7 c). Two core depths intentionally subsampled for containing fossil laminae (denoted 'f' in the graphs) contain significantly more calcite than the co-located (by depth) matrix samples devoid of fossil laminae.

5. Discussion

5.1. Mineral and organic matter associations—architecture of the microfabric

5.1.1. Distribution and morphology of minerals

SEM imagery demonstrates that the mudrocks in the Utica and Point Pleasant cores are composed of matrix laminae alternating between carbonate (m_{carb}) and phyllosilicate (m_{phyllo}) domains, with less common zones of coarse fossil (f) laminae. All identified minerals are present within the two matrix domains, including silt and clay-sized calcite, illitic clay, quartz, alkali feldspar (albite or K-feldspar), pyrite, Fe-chlorite, dolomite, and Ca-phosphate. Our XRD results and those from other studies (Wickstrom et al., 2012; Patchen and Carter, 2015; Brinkley, 2016; Worley, 2017) also indicate that the Utica Formation mudrocks generally contain a greater abundance of phyllosilicates (>50 wt. %) than those in the underlying Point Pleasant Formation, which are dominantly carbonate-bearing (>50 wt. %). Therefore, the fact that QEMSCAN mineral mapping of matrix domains (Fig. 3) returns a large area percent defined as calcite-illite phase boundaries is not surprising, as the microfabric analysis shows the strong association of platy carbonate adjacent to illitic clay folia (Fig. S8 c). Moreover, the size of many of the matrix grains (1–10 μm) is on the order of or smaller than the interaction volume for characteristic X-rays, which produces a lot of

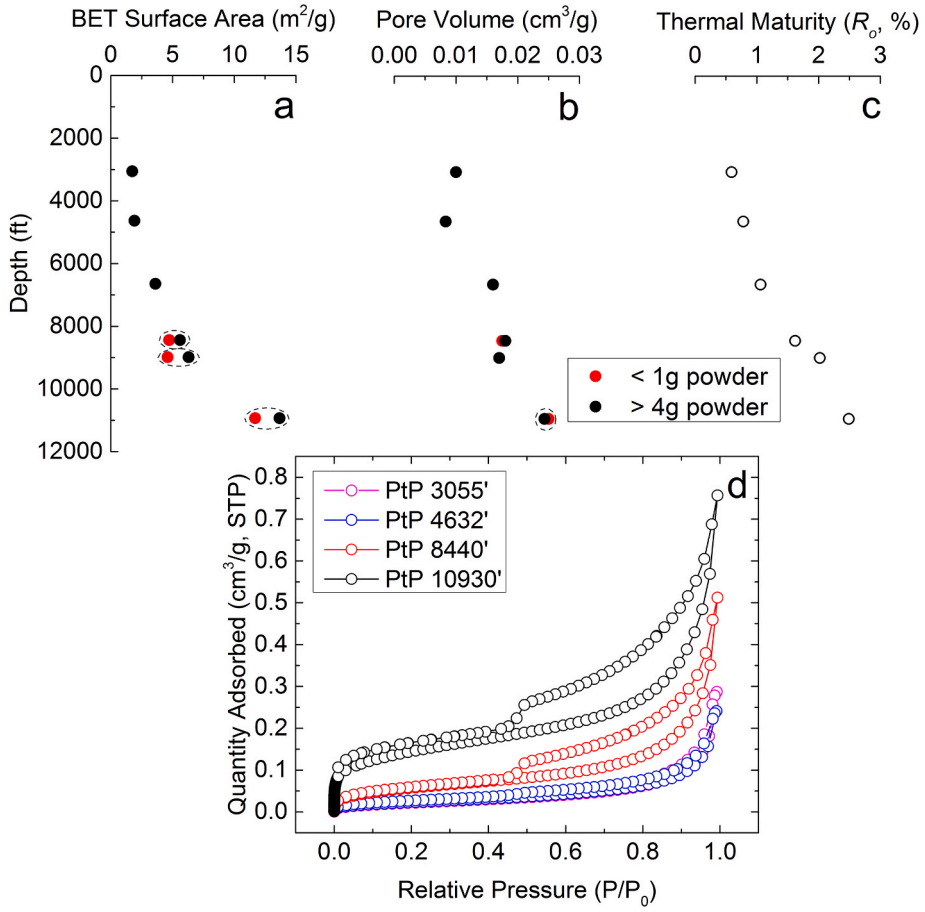

Fig. 6. a) BET surface area, **b**) pore volume, and **c)** thermal maturity with core depth. **d)** N_2 gas sorption isotherms acquired from four Point Pleasant samples of different thermal maturities. Pore volume and surface area generally increase with thermal maturity.

mixed-mineral pixels in QEMSCAN analysis.

Carbonate forms grain boundaries with illitic clay where 1) calcite cement is interwoven with the finer-grained matrix, 2) illitic folia wrap around silt- and sand-sized carbonate (grains or fossils), and 3) carbonate grains meet illite in the finest-grained, dominantly clay-sized, "pockets." These clay-sized mineral pockets within m_{carb} and m_{phyllo} are discontinuous and pinch out in both sections cut perpendicular and cut parallel to bedding. In addition to illite and calcite, clay-sized albite, feldspar, chlorite, pyrite, quartz, and calcium phosphate also are preserved in these branching, or dendritic-shaped regions, which likely formed during early depositional and cementation processes active during the late Ordovician. Silica cements also are present that would have served to resist compaction during burial, acting as a mechanical preservation mechanism for pores in the fine-grained material. Examples of bedding parallel clay pocket morphologies in the low-maturity Utica 2959 and high-maturity Point Pleasant 8440 samples are shown in Figs. 4l and 8.

As noted by Swift et al. (2014), the orientation of phyllosilicate layers in and adjacent to these pockets is controlled by clay folia that wrap around more equidimensional grains, deviating them from an otherwise bedding-parallel alignment. These observations support the interpretation that the Point Pleasant rocks, which contain ample cement (calcite, quartz) and silt-sized materials (calcite, quartz, feldspar) to hold open the clay-sized mineral and OM pockets, preserve porosity better than would a phyllosilicate-rich mudrock with a stronger tendency to undergo ductile deformation during burial.

5.1.2. *Distribution and morphology of OM*

Organic matter is widely distributed in all samples of the Utica and Point Pleasant core studied, but Individual macerals vary greatly in size, from sub-micrometer particles (Fig. 4 b, c, f) tightly intercalated among phyllosilicates and other clay sized minerals—to large, elongate macerals (up to 100s of micrometers) with long dimensions roughly parallel to bedding (Fig. 4 a, d, e). Further, there are noteworthy textural differences between large macerals and small, matrix-supported, pore-filling OM.

The aspect ratios of the large macerals, as viewed approximately perpendicular to bedding, are at least 20:1 (Fig. 4 a, d, e). This large, looping OM wraps and bends around clay-to silt-sized carbonate, quartz, and feldspar, suggesting that these mineral grains (often angular in shape) were deposited concurrently with or before the OM, which either subsequently migrated to and deposited around the mineral grains, or deformed within pore spaces as minerals recrystallized during diagenesis. According to Jacob (1989), macerals with shapes that conform to the interstices between mineral grains are secondary "migrabitumens" that moved into preexisting rock pores. This pore-filling OM is solid bitumen or pyrobitumen, depending on maturity (Hackley and Cardott, 2016; Mastalerz et al., 2018; Liu et al., 2019).

While the small, matrix-supported bitumen has migrated, it seems more plausible that the larger, seemingly intact macerals may be "OM remnants of fossils in place." Large OM objects similar to those observed in the Utica/Point Pleasant have been interpreted by some authors as algal material (Liu et al., 2017; Peng et al., 2020) ripped off of larger, shallower mats in the photic zone, and subsequently re-deposited in deeper water. Further, in an organic petrology study of the Utica Shale in Quebec, some large macerals have been identified as chitinozoans, including the recognition of structures such as chambers, oral tubes, and appendices (Ardakani et al., 2018). Some of the macerals observed in

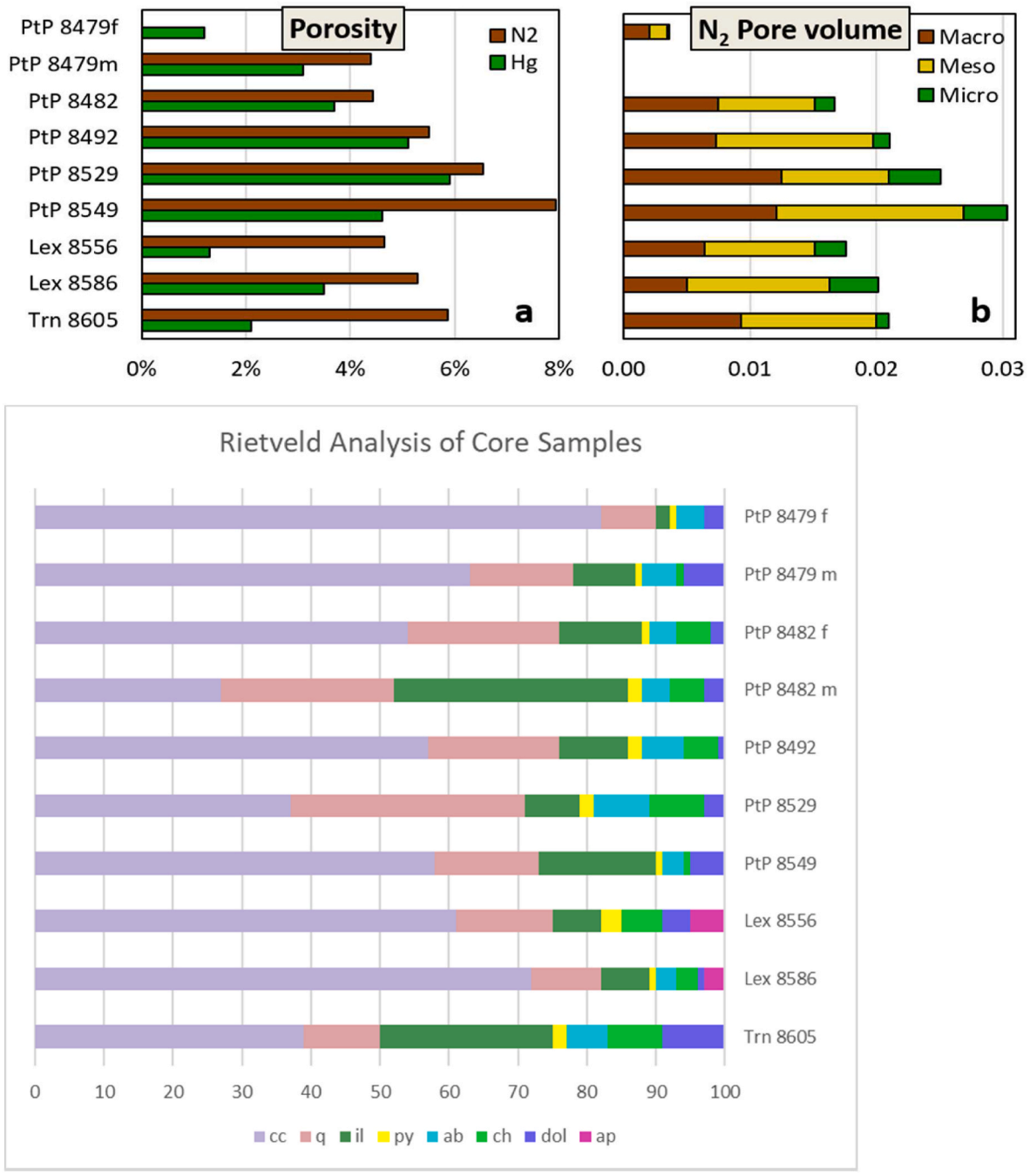

Fig. 7. a) Connected porosity (vol/vol) in Harrison County, Ohio Point Pleasant, Lexington, and Trenton/Black River Formations, as measured by N_2 gas adsorption (N_2) and mercury porosimetry (Hg). b) Connected pore volume (volume/mass, cm^3/g) distribution among macropores (>50 nm), mesopores (2–50 nm), and micropores (< 2 nm), as measured by N_2 adsorption. Sample IDs are the same for both graphs. c) Rietveld analysis of the same cores. Coarse-grained fossil skeletal laminae, detected by eye, are denoted "**f**'. "**m**" denotes fine-grained (clay and silt) matrix laminae. Mineral abbreviations: cc = calcite, q = quartz, il = illite, py = pyrite, ab = albite, ch = chlorite, dol = dolomite, ap = Ca-phosphate (apatite).

Utica and Point Pleasant core samples are similar in morphology to those described by Ardakani et al. (2018) (Fig. S12 a), although precise identification of all the large OM structures is beyond the scope of this study. Regardless of their origin, large macerals rarely contain visible pores, even in highly mature samples suggesting that either these objects do not produce gas, or gas is efficiently transported outside of their structures, preventing formation of OM porosity. This is consistent with the observations of Ardakani et al. (2018), who suggest that the specific type of OM is an important variable controlling gas generation, and that chitinozoans in particular do not contribute to the porosity observed in the Utica of southern Quebec.

The morphologies of large OM in the Utica and Point Pleasant Formations suggests that they did not migrate far, if at all, after deposition. For example, Fig. 4 e shows a large maceral almost completely enclosing silt and clay-sized grains that is likely an *in-situ* structure. Small pyrite grains and a framboid inside the loop likely were formed by sulfate-reducing microbes during early diagenesis. If such delicate structures were to envelop grains in the original carbonate muds and then move, they would likely be broken apart. On the other hand, micrometer-sized porous OM (Fig. 4 b, f), denoted "cement OM" by Camp (2015) that, depending on maturity, should be solid bitumen or pyrobitumen (Hackley and Cardott, 2016; Mastalerz et al., 2018; Liu et al., 2019) may

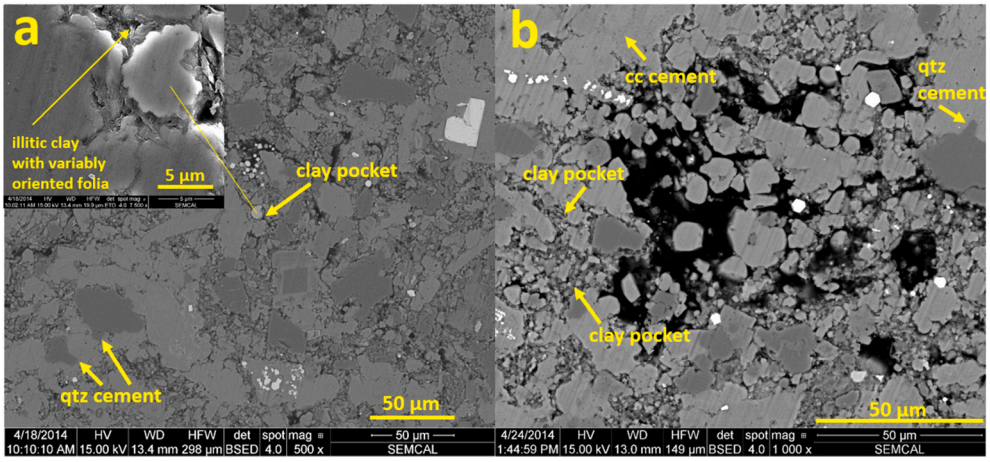

Fig. 8. Bedding-parallel sections of low-maturity Utica and high-maturity Point Pleasant cores. a) BSE image of a region containing OM (black), clay pockets, and interlocking calcite and quartz grains and cement in Ut 2959. Fine grained clay pockets (arrowed) do not polish well and, therefore, appear as variable contrast patches. OM is associated with pyrite (bright) and illitic clay folia of variable orientation (inset). b) BSE image of PtP 8440 showing a similar microfabric, although the pyrite/OM association is not as strong in this slice. Note the interlocking quartz and calcite cement in both images.

represent the once-mobile portion of the organic matter (Loucks and Reed, 2014).

5.1.3. OM-mineral-pore associations

MICP and N_2 gas sorption allow interrogation of the connected pore network of substantially larger volumes of sample than SEM, whereas the latter provides direct observation of pores in the rock microfabric. In combination then, these measurements allow association of pore size distributions with mineralogy and microfabric, at least to the SEM resolution limit. It is not always possible to assess whether pores observed by SEM are connected or unconnected, but 2D views of multiple directions in the rock fabric (e.g. parallel and perpendicular to bedding) and observations of ion-polished surfaces begin to bridge the gap.

In general, the dimensions of intra- and interparticle pores (at SEM resolution) in the Point Pleasant range from approximately 5 nm to µm-sized. Pores larger than this are attributed to core dehydration and cracking during sample preparation. SEM imagery shows the relative concentration of intraparticle pores as Ca-phosphates ≫ illitic clay and framboidal pyrite > calcite. Calcite contains the largest intraparticle pores, and Ca-phosphate and illitic clay contain the smallest. Interparticle pores in Illitic clay pockets also are a major contributor to the micrite matrix porosity along grain boundaries. Such pockets concentrate pyrite, OM, and clay "floccules" that preserve original pore space, in a manner similar to that identified in the Barnett Shale (Slatt and O'Brian, 2011).

Clay pockets viewed in bedding-parallel sections are often dendritic, and the illitic clay folia within them have variable orientations, which would tend to form pathways of pore connectivity *between* mudrock laminae (Figs. 8 a, b; S8 c, d). Illitic clay is shown wrapping around silt and clay sized grains of other minerals (which may include any of the identified minerals in the Utica/Point Pleasant suite of rocks). The BSE image in Fig. 8 a shows pyrite (bright, euhedral phase) and clay layers intimately associated with the OM. Therefore, a large fraction of the total surface area within these pockets consists of illitic-clay folia, pyrite crystallites (sometimes containing porous OM within their structures), calcite, and quartz. While some fraction of the smallest pores exists among the other clay and fine-silt sized minerals, their contribution to the pore surface area is somewhat less than the illitic clay folia.

Fig. 4 f further shows that FIB/SEM-visible meso-to macropores (up to a few hundred nm) are common in matrix-supported OM. These increase in abundance with maturity as gas evolves from the system with burial (Kuila et al., 2014), as does pore connectivity. This is particularly dramatic for the Point Pleasant (Figs. 5 and 6; Table 4).

5.2. Depositional setting

5.2.1. Formation of laminae

The mostly undisturbed, alternating laminar matrix domains (except for fossil structures that reoriented silts and clays in the original mud) (Fig. S7), indicate a quiet water, anaerobic environment with dysaerobic conditions for the fossil beds (Flügel, 2010). Nonetheless, Moore et al. (2015) suggest that the abundance of fossils in the Utica/Point Pleasant "indicate an environment that was well oxygenated much of the time." These laminae give rise to the macroscopically fissile nature of the samples, which is especially well-developed in the mature Utica and Point Pleasant cores. Although quantifying the time represented by laminar repeats is beyond the scope of this study, some authors suggest that short time intervals are represented by similarly repeating laminae in carbonate mudrocks. For example, Park and Fürsich (2001) describe mudrocks in the Tithonian Solnhofen Plattenkalk of southern Germany, in which sub-mm "layers of purely micritic limestone are rhythmically interbedded with ones of marly micritic limestone." In this case, the "relatively carbonate-poor" laminae are still 85–90 percent calcite—much richer in calcite than the m_{phyllo} observed in the Utica/Point Pleasant. Further, individual laminae of the Solnhofen span approximately 3 orders of magnitude in thickness, from 0.04 to 3 mm (40–3000 µm). Fourier spectral analysis of the laminae cycles suggest that fine-scale laminae may represent 1s of years, with variations in cyclicity attributed to climatic variations (Park and Fürsich, 2001). Due to thickness changes and cyclic patterns in the laminae over time, changes in "sedimentation regime" may also control the alternating laminae.

Another proposed mechanism for rhythmic layering of limestone and marl laminae in carbonate mudrocks is that precursor aragonite, upon becoming unstable with burial/depth, dissolves and redistributes the carbonate mineralogy *in situ*, with neo-formation of calcite (Westphal and Munnecke, 2003). This is attributed to warm water environments and could, therefore, also apply to the Utica/Point Pleasant sub-basin in the late Ordovician.

5.2.2. Sources of silt-sized grains

Within the matrix zones are silt-to clay-sized materials with angular—possibly detrital, and perhaps locally reworked—fragments of calcite, quartz, and small fossil tests, along with illitic clay, chlorite, and albite. Samples that contain abundant silt-to sand-sized grains are best described as calcisiltites (Flügel, 2010). Such textures, with relatively large, angular fragments, support a detrital origin for these grains, some of which could be intra-basinal in origin (Milliken, 2014; Peng et al., 2020). However, Robbins and Blackwelder (1992), who studied $CaCO_3$ suspensions in the Bahama banks, showed that microorganisms (algae) and organic material may serve as micro-substrates for precipitation of small, angular crystals that arrange into silt-sized spherulites. Therefore,

the possibility exists for biologically mitigated direct precipitation of lime mud from sea water, which could appear angular, and the Utica/Point Pleasant mudrocks may thus require several mechanisms to explain their depositional history.

5.2.3. Mineral paragenesis: detrital versus diagenetic phases

The mineral composition and microtexture of fine laminae influence the overall rock fabric of the Utica/Point Pleasant. This was controlled by the mineral inputs into various basin locations. It is possible that m_{phyllo} and m_{carb} pairs represent seasonal cycles, such that calm weather would favor coarsening and recrystallization of calcite and dolomite, and stormy weather would be accompanied by increased detrital inputs. Subsequent post-depositional migration and evolution of pore fluids, as well as increasing pressure and temperature with burial, also influenced the current mineralogy, and contributed to the formation of authigenic phases such as Fe-rich dolomite (Fig. S8 d) and albite (Figs. S12, S13 b).

Although diagenesis has altered the mineralogy and microfabrics of the Utica and Point Pleasant Formations to varying degrees across the sub-basin, the original matrix domains have not been completely obliterated. Fine-scale laminae are preserved, which is especially evident where the orientations of phyllosilicates change with respect to adjacent fossils (Fig. S7). Coarser, detrital silicate-rich laminae (quartz, phyllosilicates, alkali feldspar) are observed, but m_{carb} domains generally contain the largest matrix grains, partly due to the formation of early diagenetic calcite cement (Fig. S8 b). In intermediate and high-maturity samples, calcite grains are more flattened and oblong, which is likely due to space fitting and horizontal reorganization during early cementation.

The transformation of smectite to illite liberates silica, Na, Ca, Mg, and/or Fe into pore fluids, depending on the composition of the precursor clay minerals. This may have contributed to the formation of secondary quartz and dolomite cements (Milliken, 2004; Butterfield et al., 2007), although the silica could be biogenic as well. In addition, there likely was Mg, Fe and, to a certain extent, Ca exchange among clay minerals and carbonate minerals. For example, transformation of Ca and Na montmorillonite early in diagenesis would liberate Ca for calcite cement (van de Kamp, 2008). SEM analysis shows the presence of calcite/illite intergrowths, indicating neoformation of the carbonate and/or illitic clay, although determination of which is the actual replacement phase is ambiguous. During diagenesis, sodium could have been incorporated into illite interlayer sites, which is consistent with minor Na detected by EDXS analysis in the Utica/Point Pleasant clay minerals.

Both potassium- and sodium-rich feldspar phases are present in the Utica and Point Pleasant, but their concentrations are greater in the Utica. Moreover, K-feldspar is most readily detected in XRD analysis of relatively shallow/low maturity samples. Grains of detrital K-feldspar partially replaced by albite were also observed in QEMSCAN and BSE images of low-maturity sample SW 2958 (Fig. S12). These replacement rims likely formed through ion-exchange with saline pore waters. Albite abundance also is greatest in the most mature Point Pleasant sample, PtP 10,930, Table 3).

Secondary albite also occurs as euhedral silt- and clay-sized matrix grains and as a replacement of large skeletal fossils (Fig. 3), along with dolomite and quartz. The presence of euhedral authigenic albite associated with evaporites in carbonates, as well as gypsum, celestite (Fig. S13) and barite observed as replacement textures, and the relatively non-diverse fossil populations suggest formation in a hypersaline environment such as a lagoon or sabkha and/or the influence of a formation brine (Flügel, 2010). Such brines can be generated depositionally or during diagenesis (Flügel, 2010).

Considering f-domains, the presence of relatively unaltered fossil tests suggests that the original shell material was composed of low magnesium calcite. Framboidal pyrite adjacent to and between shells (Fig. S11) formed early as a result of sulfate- and/or iron-reducing bacterial activity and, because of the carbonate-rich environment, was likely limited by OM and iron availability (Berner, 1970, 1984; Coleman and Raiswell, 1993). Later in the paragenesis, fossil domains show partial replacement of the calcite tests by dolomite, quartz, pyrite and albite, mostly along fossil/matrix grain boundaries, and pyrite framboids were partially replaced by euhedral cubic or octahedral pyrite.

Shelly laminae likely posed an impediment to vertically migrating fluids, due to the way that these fossil tests stack together. However, evidence exists for enhanced early *horizontal* fluid migration locally within these layers. Pyrite framboids or micro-euhedra form linear bands in healed horizontal fractures (Fig. 4 k) and on the surfaces of fossil tests (Fig. S11). Some pyrite occurs as cubic or octahedral micro-euhedra that replaced framboids in large aggregates on the order of hundreds of microns (Fig. 3 c, d). These can form from microbial activity, or from contact between a hydrogen sulfide supersaturated fluid and an adequate iron supply (Berner, 1969; Coleman and Raiswell, 1993; Schieber, 2011; Rickard, 2012).

The most profound fabric-altering recrystallization observed is dolomitization, which obstructs connected pores in original clay- and silt-sized matrix grains in the lowest maturity Richland and Geauga County, OH samples (Table 1: Ut 2959, PtP 3055, Ut 5778, Ut 5887). Diagenetic dolomitization in these cases partly replaced the original matrix fabric, as shown by entrainment of fine-grained relict pores in secondary dolomite euhedra (Fig. S8 d). The likeliest sources of Mg and Fe for these later-stage dolomite cements are precursor clay minerals or other Fe–Mg bearing silicates; Fe oxides; illitic clay, muscovite, and pyrite comprising the clay-sized matrix particles; and early formed calcite cement. This replacement and partial obliteration of the original microfabric would be enhanced by pore fluids at dolomite/matrix domain grain boundaries. This also appears to degrade original OM, as dolomite euhedra embay and occupy space that was earlier filled with large macerals.

5.2.4. Evolution of connected porosity: Relation to paragenesis?

Porosity of organic-rich mudrocks evolves during deposition, compaction, dewatering and subsequent diagenesis. Thus, the measurements presented here reflect the combined effects of these processes on the pore network. MICP and nitrogen gas sorption measurements of several Point Pleasant samples (and underlying formations) from a single bore hole show that the highest connected porosity and surface area values are associated with the more silicate-rich Point Pleasant samples, which occur near the base of the formation. This dataset is important because this mineralogical and connected porosity relationship coincides with the hydraulic fracturing target. As noted above (Fig. 7), connected porosities increase toward the base of the Point Pleasant, and then decrease by about a third with increasing depth below the Point Pleasant in the Lexington (and Trenton/Black River).

Table 5 summarizes BET and MICP results for this high-maturity Harrison County, Ohio sample suite. The slope of the pore size distribution in the 2–3 nm region appears to be positively correlated to the abundance of phyllosilicates (illitic clay, muscovite mica), which mostly reside in the 3D-connected clay pockets (as are other clay-sized minerals and matrix-supported OM, which, therefore, also contribute to the porosity). Furthermore, these small OM (several micrometers to fractions of 1 μm) particles commonly host intraparticle pores (Loucks et al., 2012; Pahnke, 2014) that contribute to the 2–3 nm pore size signal.

Fig. S14 shows a representative isotherm and pore size distribution plot for a high-maturity, silicate-rich Point Pleasant sample near the target zone (PtP 8492) from a Harrison County borehole (Well #6). A peak at 2–3 nm in the N_2 pore size distribution plot is positively correlated to phyllosilicate (illitic clay, muscovite mica) abundance. By comparison, samples from this suite with clay-poor matrices but more carbonate cement (particularly dolomite) exhibit near constant values in this region of the pore size distribution. Similarly, MICP data obtained from silicate-rich samples show connected pore size regimes from ~2 nm to 10 nm, and another from approximately 10 nm to 50 μm (Fig. 5). In comparison, less connected porosity is measured by MICP for samples

Table 5
Porosity, pore size distribution, and pore throat size distribution for Point Pleasant, Lexington, and Trenton/Black River from a Harrison County, OH borehole.

Sample	V_{N2} (cm^3/g)	>50 nm_{N2} (cm^3/g)	2–50 nm_{N2} (cm^3/g)	<2 nm_{N2} (cm^3/g)	SA_{N2} (m^2/g)	$SA_{\mu,N2}$ (m^2/g)	$d\phi_{peak, Hg}$(nm)	$\Phi_{2nm–50\ \mu m, Hg}$ (%)	$\phi_{2–10\ nm, Hg}$ (%)
PtP 8479f	3.6E-3	2.0E-3	1.4E-3	2.3E-4	0.9	0.5	–	1.2	0.6
PtP 8479 m							3.5	3.1	2.5
PtP 8482	1.7E-2	7.4E-3	7.7E-3	1.6E-3	4.5	3.2	2.5	3.7	2.8
PtP 8492	2.1E-2	7.3E-3	1.2E-2	1.3E-3	7.0	2.9	4.9	5.1	3.5
PtP 8529	2.5E-2	1.3E-2	8.4E-3	4.1E-3	9.5	8.3	4.1	5.9	4.2
PtP 8549	3.0E-2	1.2E-2	1.5E-2	3.5E-3	8.8	7.2	3.5	4.6	3.3
Lex 8556	1.8E-2	6.4E-3	8.7E-3	2.4E-3	5.3	4.8	2.7	1.3	0.9
Lex 8586	2.0E-2	5.0E-3	1.1E-2	3.8E-3	7.8	7.5	3.5	3.5	2.4
Trn 8605	2.1E-2	9.2E-3	1.1E-2	9.4E-4	5.1	2.2	2.5	2.1	1.3

V_{N2}: Total adsorbed N_2; >50nm_{N2}: Adsorbed N_2 in macropores; 2–50nm_{N2}: Adsorbed N_2 in mesopores; <2nm_{N2}: Adsorbed N_2 in micropores; SA_{N2}: BET total surface area, N_2; $SA_{\mu,N2}$: Dubinin-Astakov micropore surface area, N_2; $d\phi_{peak, Hg}$: peak position; $\phi_{2nm–50\mu m, Hg}$: Mercury-accessible porosity through 2 nm–50 μm pore throats; $\phi_{2–10nm, Hg}$: Mercury-accessible porosity through 2–10 nm pore throats.

rich in large fossil laminae (Foley, 2016; Fig. S15) suggesting that diagenesis within these skeletal zones, primarily in the form of pyrite and carbonate recrystallization, has tightly sutured the grain boundaries. These observations support the idea that, for carbonate mudrocks, laminae mixed with silt-sized silicate particles are important contributors to connected porosity and surface area.

Qualitative analysis of Point Pleasant samples with dual beam FIB/SEM shows increasingly complex and well-developed pore structures in matrix-supported OM (e.g. bitumen, pyrobitumen) with increasing maturity, suggesting that pores in this type of OM are a major contributor to the porosity (Fig. 4 f). This is in agreement with MICP results (Fig. 5), indicating that OM-hosted porosity contributes to the connected pore network (Buchwalter, 2016). Several authors who have studied porosities and specific surface areas of OM-rich mudrocks and OM isolates note that pores in OM account for a significant fraction of the total pore system (Rexer et al., 2014; Bousige et al., 2016; Gu et al., 2016). Moreover, Rexer et al. (2014) observed that total porosities of Posidonia shale samples decreased through the oil window and then increased into the gas window, which is consistent with our MICP results. Guo and Mao (2019) showed that specific surface areas and pore volumes of Permian Shanxi shale samples "subjected to thermal simulation" decreased for Ro 0.6–2.5% and then increased for Ro>2.5%. In contrast, Zhang et al. (2018) note that in the lower Silurian Longmaxi marine shale "both the organic matter porosity and total porosity drop when entering a post-mature stage of organic matter." Measured porosities of Point Pleasant samples studied here are more sensitive to increasing maturity than are Utica samples from the same borehole (Fig. 5). Further, the deepest and most mature Point Pleasant samples (PtP 10,930, PtP 8550, PtP 8529, PtP 8440, PtP 8985) have N_2 specific surface areas from ~4 to 10-times larger than those measured for the lower maturity samples.

In a recent schematic model for the evolution of organic matter in sedimentary basins, Sanei (2020) proposed nomenclature to avoid confusion in describing types of solid bitumen in rocks, particularly for lower maturity examples. In this model, diagenetic solid bitumen results from the degradation of bituminite during diagenesis, for Ro < 0.5%, and that "initial oil solid bitumen" results from an early oil window of Ro ~0.5–0.7%. Primary oil results from thermally generated crude oil and bitumen for Ro ~0.7–1.0%, and late oil (waxy residue separated from heavy oil) for Ro ~1.0–1.4. Pyrobitumen reflects the solid resulting from continued thermal cracking of hydrocarbons in the gas window for maturities >1.4% Ro (Sanei, 2020). He noted that the type of OM is important, and that an "increase in quantity of oil prone organic matter would lead to forming a network of bitumen, and hence a more pervasive distribution within the pore network of the rock" (Sanei, 2020). With this in mind, it is possible that the higher maturity (gas window) samples studied here reflect the further opening of available pore space in the network defined by the clay pockets and bedding plane partings (Lewan, 1987).

Only the lowest maturity Chesapeake pair (Ut 2959′ and PtP 3055′) shows essentially the same MICP results for both Utica and Point Pleasant, which may reflect their location at the northern sub-basin margin (Fig. 1, Well #1). The relatively high calcite and dolomite content measured for both samples (Table 3, XRD dataset 2) may thus reflect a different initial mineralogical sediment composition resulting from closer proximity to the flanking Trenton carbonate platform. Moreover, for sample pairs located toward the eastern part of the basin, elevated Fe-fluorescence in XRD scans of Utica samples relative to Point Pleasant samples is observed. This observation points to the Taconic Highland to the east as the likeliest contributor of a greater flux of Fe into the sub-basin. Therefore, it is acknowledged that specific borehole position with respect to geographic location within the sub-basin would tend to exert a control on mineralogy and ultimately pore evolution.

Erenpreiss (2015) noted that there are no direct correlations between TOC data and spectral gamma-ray (SGR) log signatures acquired from core samples of the Utica and Point Pleasant Formations, and that GR intensity is dominated by potassium. This observation suggests that high OM is not necessarily correlated with high potassium, which would reside mostly in hydrous phyllosilicates (illitic clay, muscovite mica). However, as ion-polished rocks clearly show a strong association between pores and matrix-supported OM (Fig. 4 b, f), it is clear that rocks containing the most phyllosilicates are not necessarily the best for hydrocarbon recovery. In fact, connected porosity (as measured with both MICP and N_2 gas sorption) is greatest in calcite-rich Point Pleasant samples, and increases dramatically with burial/maturity. Thus, porous OM may exist in a rock, but the rock matrix must also support efficient fracture generation. In addition, our results show that large OM grains, which presumably contribute a significant portion of TOC, are strongly associated with carbonates and quartz as well as illitic clay, explaining why OM content does not correlate with increased spectral gamma-ray log intensity.

Point Pleasant specific surface areas, as measured by N_2 gas sorption, are lower in lower-maturity core samples (Table 4, Fig. 6). This is consistent with the observation of low maturity Utica and Point Pleasant exhibiting a more isotropic character to the fabric, both parallel and perpendicular to bedding, and indicates that dolomitization tends to transition an otherwise laminar mudrock architecture to one that is more interlocking, disrupting connected pore networks. Dewhurst et al. (1999) suggest that grain size distributions and grain shape on the core scale, followed by laminar structure (fabric alignment and compaction), and diagenetic overprinting are the main variables controlling mudrock permeability. This is because diagenetic carbonate such as euhedral dolomite (Fig. S8 d) or recrystallized fossil laminae composed of very coarse—but interlocking—crystals (Fig. S15) each contribute to lower connected porosity. Therefore, the degree of cementation appears to be a significant control on the connected porosity, as measured in the Utica/Point Pleasant core samples in this study.

Patchen et al. (2006) discuss the influence of various types of dolomitization in the Lexington/Trenton Formation on hydrocarbon

reservoir quality. In particular, they suggest that vuggy "hydrothermal dolomite" forms as a result of deep-seated brine fluid migration along faults, and locally increases porosity and permeability. However, these authors also note that, overall, dolomitzation served to decrease porosity. This is important for the Utica/Point Pleasant, although carbonates (mainly as early calcite cement and detrital grains) also helped preserve matrix porosity by providing elevated strength and resistance to burial compaction. Zhao et al. (2017) discuss the importance of pore filling calcite and dolomite for inhibiting compaction, yet decreasing the overall porosity in CARL mudrock lithologies of the Wufeng and Longmaxi Shale.

6. Conclusions

Analysis of porosity and pore size distribution in the Utica/Point Pleasant Formation as a function of mineralogy, microfabric, and maturity provides a foundation for understanding the evolution of the pore architecture of this important energy resource. Based on direct (imaging) and indirect (MICP, N_2 gas sorption) measurements of pores, and bulk and microanalysis of minerals, the results reflect the relative degree of diagenetic cementation that has either enhanced or occluded primary porosity, and the differences in quality and quantity of connected porosity in pockets of fine silt- and clay-sized materials, especially those with matrix-supported organic matter (bitumen, pyrobitumen).

Considering diagenesis, early calcite and quartz cementation preserved primary porosity in the rock matrix by increasing the strength of mudrock laminae. An adequate quantity of phyllosilicates also was important early in the system, as clay/OM floccules tend to protect organic matter from degradation. Small-scale microfabric components (i.e., clay pockets) that were not replaced with cements remained open, allowing for infilling of clay- and fine silt-sized carbonates, silicates, phosphates, sulfides, and OM. Conversely, late-stage dolomitization, which is most prevalent in the lower maturity core samples studied, tends to occlude porosity by directly replacing material in the clay pockets. Recrystallization of coarse fossil laminae during diagenesis locally occludes the pore network, and these layers would serve as inhibitors of fluid movement perpendicular to bedding.

The presence of silt- and sand-sized grains in matrix laminae enhance the connected porosity in the core samples. These coarse, brittle, and equant-shaped grains (calcite, quartz, pyrite) facilitated preservation of fluid pathways by opening up pore spaces as elastic phyllosilicate folia wrapped around them. In addition, SEM and HIM imagery demonstrated that pores developed in OM are important contributors to overall pore connectivity. Organic pores mostly reside in small, matrix-supported OM (bitumen, pyrobitumen), which in turn have been preserved in the dendritic, small grain-sized clay pockets by calcite and quartz cementation during early diagenesis.

The highest measured surface areas and pore volumes are associated with high maturity Point Pleasant core samples, and also include samples with the highest phyllosilicate and quartz contents. Further, connected porosities in core vertically sampled from Well #13 increase toward the base of the Point Pleasant and in the vicinity of the target interval for hydraulic fracturing. In contrast, the lowest measured surface areas and pore volumes measured are from the more shallow, lowest maturity samples and for which dolomitization is most prevalent in the microfabric. Mercury-accessible porosity also is low for subsamples of core containing abundant fossil-rich laminae.

Carbonates exhibit a platy morphology similar to phyllosilicates, and they contribute to the dominantly bedding plane-parallel fractures observed in Utica/Point Pleasant mudstones, from the hand sample to the thin section scale. Indeed, much of the Point Pleasant matrix is composed of intimately interwoven illitic clay and calcite cement. This suggests that open space (e.g., channel pores as defined by Pahnke, 2014) parallel or subparallel to carbonate cements may provide important pathways for fluids. High Sr levels measured in flowback/produced (FP) fluids derived from the Point Pleasant in Harrison County, Ohio, with Sr/Cl ratios approximately two orders of magnitude greater than seawater (Welch et al., 2021) may reflect solubilization of such carbonate.

At all maturities studied, fluid migration pathways, which exhibit greater porosity parallel to bedding surfaces than perpendicular to bedding (Swift et al., 2014), involve boundaries between matrix carbonates and phyllosilicates. Fluid would access such horizontal breaks (grain boundaries or natural fractures) parallel to matrix laminae. Pockets of clay-to-silt-sized materials (minerals and OM), in turn, would then serve to connect laminae, contributing to three-dimensional flow pathways in these rocks.

Declaration of competing interest

The authors declare that they have no known competing financial interests or personal relationships that could have appeared to influence the work reported in this paper.

Acknowledgements

ERB, SAW, and JMS received partial support from the National Science Foundation Dimensions of Biodiversity (award no. EAR-1847684). Work was also supported by our industry partners, Chesapeake Energy and Gulfport Energy. TL and DRC received partial support from the U.S. Department of Energy, Office of Basic Energy Sciences, under Contract No. DE-SC0006878 (Division of Chemical Sciences, Geosciences, and Biosciences), Geosciences Program. Work by JMS and AMS at the Molecular Foundry was supported by the Office of Science, Office of Basic Energy Sciences, of the U.S. Department of Energy under Contract No. DE-AC02-05CH11231. We thank Adam J. Rondinone for help with the helium ion microscopy conducted at the Center for Nanophase Materials Sciences, which is a DOE Office of Science User Facility at Oak Ridge National Laboratory. AMS, SAW and JMS were participants in the CNMS User Program, proposal CNMS2016-109. Work by LMA was supported by the U.S. Department of Energy, Office of Science, Office of Basic Energy Sciences, Chemical Sciences, Geosciences, and Biosciences Division. Sample analyses at the Ohio State University were done in the Subsurface Energy Materials Characterization and Analysis Laboratory (SEMCAL). We thank the Ohio Geological Survey, and in particular the late Gregory A. Schumacher, for help with obtaining core samples, and Dustin Crandall from NETL for providing XCT imagery of core samples. This manuscript benefitted from the careful review of T.J. Kneafsey at LBNL and two anonymous reviewers. The authors state that they have no conflicts of interest to declare.

Appendix A. Supplementary data

Supplementary data to this article can be found online at https://doi.org/10.1016/j.marpetgeo.2021.105345.

Author statement

Julia M. Sheets: Writing – original draft preparation, Methodology, Visualization, Investigation, Formal analysis, Validation, Conceptualization, Data curation, Writing- Reviewing and Editing. **Susan A. Welch:** Investigation, Writing- Reviewing and Editing, Validation, Conceptualization, Methodology, Data curation. **Tingting Liu:** Investigation, Formal analysis, Validation, Visualization, Writing- Reviewing and Editing Investigation. **Edwin R. Buchwalter:** Investigation, Methodology, Formal analysis, Validation, Writing- Reviewing and Editing. **Alexander M. Swift:** Investigation, Methodology, Formal analysis, Validation, Writing- Reviewing and Editing. **Steve Chipera:** Resources, Investigation, Formal analysis, Validation, Data curation, Software, Writing- Reviewing and Editing. **Lawrence M. Anovitz:** Conceptualization, Resources, Writing- Reviewing and Editing. **David R. Cole:**

Conceptualization, Supervision, Resources, Funding acquisition, Methodology, Project administration, Writing- Reviewing and Editing.

References

Anovitz, L.M., Cole, D.R., Jackson, A.J., Rother, G., Littrell, K.C., Allard, L.F., Pollington, A.D., Wesolowski, D.J., 2015. Effect of quartz overgrowth precipitation on the multiscale porosity of sandstone: A (U)SANS and imaging analysis. Geochim. Cosmochim. Acta 158, 199–222.

Ardakani, H.O., Sanei, H., Ghanizadeh, A., Lavoie, D., Chen, Z., Clarkson, C.R., 2018. Do all fractions of organic matter contribute equally in shale porosity? A case study from Upper Ordovician Utica Shale, southern Quebec, Canada. Marine Petrol. Geol. 92, 794–808.

Baturin, G.N., 1981. Phosphorite on the ocean shelves. In: Developments in Sedimentology, vol. 33. Baturin. https://doi.org/10.1016/S0070-4571(08)70317-0.

Berner, R.A., 1984. Sedimentary pyrite formation: an update. Geochem. Cosmochim. Acta 48, 605–615. https://doi.org/10.1016/0016-7037(84)90089-9.

Berner, R.A., 1970. Sedimentary pyrite formation. Am. J. Sci. 268, 1–23.

Berner, R.A., 1969. The synthesis of framboidal pyrite. Econ. Geol. 64, 383–384.

Bloxson, J., 2017. Mineralogical and Facies Variations within the Utica Shale, Ohio Using Visible Derivative Spectroscopy, Principle Component Analysis, and Multivariate Clustering. PhD dissertation. Case Western Reserve University.

Bousige, C., Ghimbeu, C.M., Vix-Guteri, C., Pomerantz, A.E., Suleimenova, A., Vaughan, G., Garbarino, G., Feygenson, M., Wildgruber, C., Ulm, F.-J., Pellenq, R.J.-M., Coasne, B., 2016. Realistic molecular model of kerogen's nanostructure. Nat. Mater. 15, 576–582. https://doi.org/10.1038/NMAT4541.

Brinkley, S.A., 2016. Petroleum Geology of the Utica/Point Pleasant Play in Washington County, Ohio: MS Thesis. East Carolina University, p. 61.

Buchwalter, E.R., Swift, A.M., Sheets, J.M., Cole, D.R., Prisk, T., Anovitz, L., Ilavsky, M., Rivers, S., Welch, S., Chipera, S., 2015. Mapping of microbial habitats in organic-rich shale. In: Unconventional Resources Technology Conference (URTeC), San Antonio, Texas, USA, 20–22 July. https://doi.org/10.15530/urtec-2015-2174226.

Buchwalter, E.R., 2016. The Geochemical and Spatial Argument for Microbial Life Surviving into Early Diagenesis in the Appalachian Basin. MS Thesis. The Ohio State University. OhioLINK Electronic Theses and Dissertations Center. https://etd.ohiolink.edu.

Bustin, A.M.M., Bustin, R.M., 2012. Importance of rock properties on the producibility of gas shales. Int. J. Coal Geol. 103, 132–147.

Butterfield, N.J., Balthasar, U., Wilson, L.A., 2007. Fossil diagenesis in the burgess shale. Palaeontology 50 (3), 537–543.

Camp, W.K., 2015. Extended abstract: diagenetic evolution of organic matter cements in unconventional shale reservoirs. Houston Geol. Soc. Bull. 58 (3), 11–13.

Coleman, M.L., Raiswell, R., 1993. Microbial mineralization of organic matter: mechanisms of self-organization and inferred rates of precipitation of diagenetic minerals. Phil. Trans. Roy. Soc. Lond. 344, 69–87.

Dewhurst, D.N., Yang, Y., Aplin, A.C., 1999. Permeability and fluid flow in natural mudstones. In: Aplin, A.C., Fleet, A.J., Macquaker, J.H.S. (Eds.), Muds and Mudstones: Physical and Fluid Flow Properties, vol. 158. Geological Society of London Special Publications, pp. 23–43.

EIA Drilling Productivity Report, November 2020.

EIA Monthly Energy Review, November 2020.

EIA Ohio Dry Natural Gas Production, accessed December 2020 (https://www.eia.gov/dnav/ng/hist/na1160_soh_2a.htm).

EIA Weekly US Field Production of Crude oil, accessed January 2021 (https://www.eia.gov/dnav/pet/hist/LeafHandler.ashx?n=PET&s=WCRFPUS2&f=W).

Erenpreiss, M.S., 2015. High resolution core photography and spectral gamma-ray logging. In: Patchen, D.G., Carter, K.M. (Eds.), A Geologic Play Book for Utica Shale Appalachian Basin Exploration, Final Report of the Utica Shale Appalachian Basin Exploration Consortium, pp. 36–49. Available from: http://www.wvgs.wvnet.edu/utica.

Ettensohn, F.R., 2008. The appalachian foreland basin in eastern United States. In: Miall, A.D. (Ed.), Sedimentary Basins of the World, vol. 5. The Sedimentary Basins of the United States and Canada, pp. 105–179. https://doi.org/10.1016/S1874-5997(08)00004-X.

Ettensohn, F.R., 2010. Origin of Late Ordovician (Mid-mohawkian) Temperate-Water Conditions on Southeastern Laurentia: Glacial or Tectonic, vol. 466. Geological Society of America Special Paper, pp. 163–175.

Faill, R.T., 1997. A geologic history of the north-central Appalachians. Part 1. Orogenesis from the Mesoproterozoic through the Taconic orogeny. Am. J. Sci. 297, 551–619.

Fairbanks, M.D., Ruppel, S.C., Rowe, H., 2016. High resolution stratigraphy and facies architecture of the upper Cretaceous (Cenomanian–Turonian) eagle Ford group. Central Texas: AAPG (Am. Assoc. Pet. Geol.) Bull. 100 (3), 379–403. https://doi.org/10.1306/12071514187.

Flügel, E., 2010. Microfacies of Carbonate Rocks, Analysis, Interpretation and Application. Springer, Heidelberg Dordrecht London New York, ISBN 978-3-642-03795-5. https://doi.org/10.1007/10.1007/978-3-642-03796-2 (Print) 978-3-642-03796-2 (Online).

Foley, D.J., 2016. Analysis of the Point Pleasant/Lexington/Trenton Formations: Sulfides, Mineralogy, and Trace Elements as Geochemical Proxies: MS Thesis. The Ohio State University, p. 102.

Folk, R.L., 1959. Practical classification of limestones. AAPG (Am. Assoc. Pet. Geol.) Bull. 43, 1–38.

Folk, R.L., 1962. Spectral subdivision of limestone types. In: Ham, W.E. (Ed.), Classification of Carbonate Rocks, vol. 1. AAPG Memoir, pp. 62–84.

Furmann, A., Mastalerz, M., Bish, D., Schimmelmann, A., Pedersen, P.K., 2016. Porosity and pore size distribution in mudrocks from the Belle Fourche and second white specks formations in Alberta, Canada. AAPG (Am. Assoc. Pet. Geol.) Bull. 100 (8), 1265–1288.

Guo, S., Mao, W., 2019. Division of diagenesis and pore evolution of a Permian Shanxi shale in the Ordos basin, China. J. Petrol. Sci. Eng. 182, 106351. https://doi.org/10.1016/j.petrol.2019.106351.

Gu, X., Mildner, D.F.R., Cole, D.R., Rother, G., Slingerland, R., Brantley, S.L., 2016. Quantification of organic porosity and wettability in Marcellus shale using ultra-small and small angle neutron scattering. Energy Fuel. 30, 4438–4449.

Hackley, P.C., Cardott, B.J., 2016. Application of organic petrography in North American shale petroleum systems: a review. Int. J. Coal Geol. 163, 8–51.

Hickman, J., Eble, C., Harris, D., 2015. Subsurface mapping and correlation through geophysical log analysis. In: Patchen, D.G., Carter, K.M. (Eds.), A Geologic Play Book for Utica Shale Appalachian Basin Exploration, Final Report of the Utica Shale Appalachian Basin Exploration Consortium, pp. 22–35. Available from: http://www.wvgs.wvnet.edu/utica.

Jacob, H., 1989. Classification, structure, genesis and practical importance of natural solid oil bitumen (migrabitumen"). Int. J. Coal Geol. 11, 65–79.

Jarvie, D.M., Claxton, B.L., Henk, F., Breyer, J.T., 2001. Oil and Shale Gas from the Barnett Shale. Ft. Worth Basin, Texas. Talk Presented at the AAPG National Convention. American Association of Petroleum Geologists Bulletin A., Denver, CO', p. 100.

Kolata, D.R., Huff, W.D., Bergstrom, S.M., 2001. The Ordovician Sebree Trough: an oceanic passage to the midcontinent United States, 113. Geological Society of America Bulletin, pp. 1067–1078.

Kuila, U., McCarty, D.K., Derkowski, A., Fischer, T.B., Topor, T., Prasad, M., 2014. Nano-scale texture and porosity of organic matter and clay minerals in organic-rich mudrocks. Fuel 135, 359–373. https://doi.org/10.1016/j.fuel.2014.06.036.

Kuila, U., Prasad, M., 2013. Specific surface area and pore-size distribution in clays and shales. Geophys. Prospect. 61 (2), 341–362.

Kuila, U., 2013. Measurement and Interpretation of Porosity and Pore Size Distribution in Mudrocks: the Hole Story of Shales. PhD Dissertation. Colorado School of Mines.

Lazar, O.R., Bohacs, K.M., Macquaker, J.H.S., Schieber, J., Demko, T.M., 2015. Capturing key attributes of fine-grained sedimentary rocks in outcrops, cores, and thin sections: nomenclature and description guidelines. J. Sediment. Res. 85 (3), 230–246. https://doi.org/10.2110/jsr.2015.11.

Lewan, M.D., 1987. Petrographic study of primary petroleum migration in the Woodford Shale and related rock units. In: Doligez, B. (Ed.), Migration of Hydrocarbons in Sedimentary Basins, pp. 113–130.

Liu, B., Schieber, J., Mastalerz, M., 2017. Combined SEM and reflected light petrography of organic matter in the New Albany Shale (Devonian-Mississippian) in the Illinois Basin: a perspective on organic pore development with thermal maturation. Int. J. Coal Geol. 184, 57–72.

Liu, B., Schieber, J., Mastalerz, M., 2019. Petrographic and micro-FTIR study of organic matter in the Upper Devonian New Albany Shale during thermal maturation: implications for kerogen transformation. In: Camp, W., Milliken, K., Taylor, K., Fishman, N., Hackley, P., Macquaker, J. (Eds.), Mudstone Diagenesis: Research Perspectives for Shale Hydrocarbon Reservoirs, Seals, and Source Rocks. AAPG Memoir 120, pp. 165–188.

Loucks, R.G., Reed, R.M., Ruppel, S.C., Hammes, U., 2012. Spectrum of pore types and networks in mudrocks and a descriptive classification for matrix-related mudrock pores. AAPG (Am. Assoc. Pet. Geol.) Bull. 96 (6), 1071–1098.

Loucks, R.G., Reed, R.M., 2014. Scanning-electron microscope petrographic evidence for distinguishing organic matter pores associated with depositional organic matter versus migrated organic matter in mudrocks. GCAGS J. 3, 51–60.

Mac Kinnon, M.A., Brouwer, J., Samuelsen, S., 2018. The role of natural gas and its infrastructure in mitigating greenhouse gas emissions, improving regional air quality, and renewable resource integration. Prog. Energy Combust. Sci. 64, 62–92. https://doi.org/10.1016/j.pecs.2017.10.002.

Macquaker, J.H.S., Adams, A.E., 2003. Maximizing information from fine-grained sedimentary rocks: an inclusive nomenclature for mudstones. J. Sediment. Res. 73 (5), 735–744, 10.1306/012203730735.

Mastalerz, M., Hampton, L., Drobniak, A., Loope, H., 2017. Significance of analytical particle size in low-pressure N_2 and CO_2 adsorption of coal and shale. Int. J. Coal Geol. 178, 122–131.

Mastalerz, M., Drobniak, A., Stankiewicz, A.B., 2018. Origin, properties, and implications of solid bitumen in source-rock reservoirs: a review. Int. J. Coal Geol. 195, 14–36.

Milliken, K.L., 2004. Elemental transfer in sandstone-shale sequences: chapter 5. In: Mackenzie, F.T. (Ed.), Sediments, Diagenesis, and Sedimentary Rocks, vol. 7. Treatise on Geochemistry, Elsevier, pp. 159–190.

Milliken, K.L., 2014. A compositional classification for grain assemblages in fine-grained sediments and sedimentary rocks. J. Sediment. Res. 84, 1185–1199.

Moore, J., Pool, S., Bocan, J., Saucer, J., 2015. Introduction and Purpose – Utica Shale play book study website. In: Patchen, D.G., Carter, K.M. (Eds.), A Geologic Play Book for Utica Shale Appalachian Basin Exploration, Final Report of the Utica Shale Appalachian Basin Exploration Consortium, pp. 1–11. Available from: http://www.wvgs.wvnet.edu/utica.

Pahnke, P.D., 2014. Characterization of Cretaceous Chalk Microporosity Related to Depositional Texture: Based upon Study of the Upper Cretaceous Niobrara Formation, Denver Julesburg Basin, Colorado and Wyoming: Master's Thesis. Brigham Young University, Provo, Utah, p. 52.

Patchen, D.G., Hickman, J.B., Harris, D.C., Drahozval, J.A., Lake, P.D., Smith, L.B., Nyahay, R., Schulze, R., Riley, R.A., Baranoski, M.T., Wickstrom, L.H., Laughrey, C. D., Kostelnik, J., Harper, J.A., Avary, K.L., Bocan, J., Hohn, M.E., McDowell, R.,

2006. A Geologic Play Book for Trenton-Black River Appalachian Basin Exploration: U.S. Department of Energy, Final Report, Contract Number DE-FC-03NT41856, 582 P. Rep. Morgantown. West Virginia University Research Corporation, 2006. Print.
A geologic play book for Utica Shale Appalachian basin exploration, Final report of the Utica Shale Appalachian basin exploration consortium. In: Patchen, D.G., Carter, K. M. (Eds.), 2015, p. 187 p. Available from: http://www.wvgs.wvnet.edu/utica.
Park, M.-H., Fürsich, 2001. Cyclic nature of lamination in the Tithonian Solnhofen Plattenkalk of southern Germany and its palaeoclimatic implications. Int. J. Earth Sci. (Geol Rundsch) 90, 847–854. https://doi.org/10.1007/s005310000191.
Peng, J., Milliken, K., Fu, Q., Janson, X., Hamlin, H.S., 2020. Grain assemblages and diagenesis in organic-rich mudrocks, upper Pennsylvanian cline shale (Wolfcamp D), Midland basin, Texas. AAPG (Am. Assoc. Pet. Geol.) Bull. 104 https://doi.org/10.1306/03022018240.
Potter, P.E., 2007. Exploring the Geology of the Cincinnati/northern Kentucky Region, Kentucky Geological Survey Special Publication No., vol. 8. Series XII, p. 128.
Raimi, D., 2020. The greenhouse gas effects of increased US oil and gas production. Energy Trans. 4, 45–56. https://doi.org/10.1007/s41825-020-00022-1.
Rexer, T.F., Mathia, E.J., Aplin, A.C., Thomas, K.M., 2014. High-pressure methane adsorption and characterization of pores in Posidonia Shales and isolated kerogens. Energy Fuel. 28, 2886–2901 dx.doi.org/10.1021/ef402466m.
Rickard, D., 2012. Sulfidic Sediments and Sedimentary Rocks, vol. 65. Developments in Sedimentology.
Robbins, L.L., Blackwelder, P.L., 1992. Biochemical and ultrastructural evidence for the origin of whitings: a biologically induced calcium carbonate precipitation mechanism. Geology 20, 464–468.
Rouquerol, J., Rouquerol, F., Sing, K.S.W., 1998. Adsorption by Powders and Porous Solids. Academic press, p. 467.
Sanei, H.S., 2020. Genesis of solid bitumen. Nat. Sci. Rep. 10, 1–10. https://doi.org/10.1038/s41598-020-72692-2.
Schieber, J., 2011. Iron sulfide formation. In: Reitner, J., Thiel, V. (Eds.), Encyclopedia of Geobiology. Springer, pp. 486–502.
Sieminski, A., 2014. EIA International Energy Outlook 2014. for Columbia University Center on Global Energy Policy. https://www.eia.gov/pressroom/presentations/sieminski_09222014_columbia.pdf. (Accessed 22 September 2014).
Sing, K.S.W., Everett, D.H., Haul, R.A.W., Moscou, L., Pierotti, R.A., Rouquerol, J., Siemieniewska, T., 1985. Reporting physisorption data for gas/solid systems with special reference to the determination of surface area and porosity, IUPAC physical chemistry division, commission on colloid and surface chemistry including catalysis*. Pure Appl. Chem. 57 (4), 603–619.
Slatt, R.M., O'Brian, N.R., 2011. Pore Types in the Barnett and Woodford Gas Shales: Contribution to Understanding Gas Storage and Migration Pathways in Fine-Grained Rocks: AAPG Search and Discovery Article #80166. Houston, TX, April 10–13 2011.
Swift, A., Sheets, J., Cole, D., Anovitz, L., Welch, S., Gu, X., Mildner, D., Chipera, S., Buchwalter, E., Cook, A., 2014. Nano- to microscale pore characterization of the Utica Shale. In: Unconventional Resources Technology Conference (URTeC), Denver, CO 25–27 August. https://doi.org/10.151530/urtec-2014-1923522.
Thommes, M., Kaneko, K., Neimark, A.V., Olivier, F.R.-R., Rouquerol, J., Sing, K.S.W., 2015. Physisorption of gases, with special reference to the evaluation of surface area and pore size distribution, IUPAC Technical Report. Pure Appl. Chem. 87 (9–10), 1051–1069. https://doi.org/10.1515/pac-2014-1117.
van de Kamp, P.C., 2008. Smectite-illite-muscovite transformations, quartz dissolution, and silica release in shales. Clay Clay Miner. 56, 66–81. https://doi-org.proxy.lib.ohio-state.edu/10.1346/CCMN.2008.0560106.
Welch, S.A., Sheets, J.M., Daly, R.A., Hanson, A., Sharma, S., Darrah, T., Olesik, J., Lutton, A., Mouser, P.J., Wrighton, K.C., Wilkins, M.J., Carr, T., Cole, D.R., 2021. Comparative geochemistry of flowback chemistry from the utica/point pleasant and Marcellus formations. Chem. Geol. https://doi.org/10.1016/j.chemgeo.2020.120041.
Westphal, H., Munnecke, A., 2003. Limestone-marl alternations: a warm-water phenomenon? Geology 31 (3), 263–266.
Wickstrom, L.H., Gray, J.D., Stieglitz, R.D., 1992. Stratigraphy, structure, and production history of the Trenton Limestone (Ordovician) and adjacent strata in northwestern Ohio. Ohio Geol. Surv. Rep. Invest. 143, 78.
Wickstrom, L., Riley, R., Erenpreiss, M., Perry, C., 2012. Geologic Overview and Activity Update for the Utica-Point Pleasant Shale Play in Ohio. Search and Discovery Article #10409 Posted June 25, 2012 *Adapted from Poster Presentation at AAPG Annual Convention and Exhibition, Long Beach, California. April 22–25, 2012. http://www.searchanddiscovery.com/pdfz/documents/2012/10409wickstrom/ndx_wickstrom.pdf.html.
Witt, W.D., 1993. Chapter 1 Principal Oil and Gas Plays in the Appalachian Basin (Province 131) Middle Eocene Intrusive Igneous Rocks of the Central Appalachian Valley and Ridge Province—Setting, Chemistry, and Implication for Crustal Structure. U.S.G.S. Survey Bulletin, p. 1839-I.
Witzke, B.J., 1990. Palaeoclimatic Constraints for Palaeozoic Palaeolatitudes of Laurentia and Euramerica, vol. 12. Geological Society, London, Memoires, pp. 57–73. https://doi.org/10.1144/GSL.MEM.1990.012.01.05.
Worley, D., 2017. Coupled Geochemical and Nano-Petrophysical Study of the Utica Play, Appalachian Basin. MS Thesis. The University of Texas at Arlington, Ohio, USA.
Zhao, J., Jin, Z., Jin, Z., Hu, Q., Hu, Z., Du, W., Yan, C., Geng, Y., 2017. Mineral types and organic matters of the Ordovician-Silurian Wufeng and Longmaxi Shale in the Sichuan Basin, China: implications for pore systems, diagenetic pathways, and reservoir quality in fine-grained sedimentary rocks. J. Mar. Petrol. Geol. 86, 655–674. https://doi.org/10.1016/j.marpetgeo.2017.06.031.
Zhang, L., Li, B., Jiang, S., Xiao, D., Lu, S., Zhang, Y., Gong, C., Chen, L., 2018. Heterogeneity characterization of the lower Silurian Longmaxi marine shale in the Pengshui area, South China. Int. J. Coal Geol. 195, 250–266. https://doi.org/10.1016/j.coal.2018.05.015.